

Multilayered Atomic Relaxation in van der Waals Heterostructures

Dorri Halbertal^{1,*}, Lennart Klebl^{2,*}, Valerie Hsieh¹, Jacob Cook,³ Stephen Carr,⁴ Guang Bian,³ Cory R. Dean,¹ Dante M. Kennes^{2,5} and D. N. Basov¹

¹*Department of Physics, Columbia University, New York, New York 10027, USA*

²*Institut für Theorie der Statistischen Physik, RWTH Aachen University and JARA-Fundamentals of Future Information Technology, 52056 Aachen, Germany*

³*Department of Physics and Astronomy, University of Missouri, Columbia, Missouri 65211, USA*

⁴*Physics Department, Brown University, Providence, Rhode Island 02912, USA*

⁵*Max Planck Institute for the Structure and Dynamics of Matter, Center for Free Electron Laser Science, 22761 Hamburg, Germany*

 (Received 22 June 2022; revised 7 November 2022; accepted 10 January 2023; published 27 February 2023)

When two-dimensional van der Waals materials are stacked to build heterostructures, moiré patterns emerge from twisted interfaces or from a mismatch in the lattice constant of individual layers. Relaxation of the atomic positions is a direct, generic consequence of the moiré pattern, with many implications for the physical properties. Moiré-driven atomic relaxation may be naively thought to be restricted to the interfacial layers and thus irrelevant for multilayered heterostructures. However, we provide experimental evidence for the importance of the three-dimensional nature of the relaxation in two types of van der Waals heterostructures: First, in multilayer graphene twisted on graphite at small twist angles ($\theta \approx 0.14^\circ$), we observe propagation of relaxation domains even beyond 18 graphene layers. Second, we show how for multilayer PdTe₂ on Bi₂Se₃ the moiré lattice constant depends on the number of PdTe₂ layers. Motivated by the experimental findings, we develop a continuum approach to model multilayered relaxation processes based on the generalized stacking fault energy functional given by *ab initio* simulations. Leveraging the continuum property of the approach enables us to access large-scale regimes and achieve agreement with our experimental data for both systems. Furthermore, it is well known that the electronic structure of graphene sensitively depends on local lattice deformations. Therefore, we study the impact of multilayered relaxation on the local density of states of the twisted graphitic system. We identify measurable implications for the system, experimentally accessible by scanning tunneling microscopy. Our multilayered relaxation approach is not restricted to the discussed systems and can be used to uncover the impact of an interfacial defect on various layered systems of interest.

DOI: [10.1103/PhysRevX.13.011026](https://doi.org/10.1103/PhysRevX.13.011026)

Subject Areas: Condensed Matter Physics, Graphene, Mesoscopics

I. INTRODUCTION

Moiré van der Waals (vdW) heterostructures have drawn considerable interest in the past few years. Whenever two layers with relative twist or lattice mismatch are stacked, large-scale periodic perturbations of stacking configurations emerge. So-called moiré superlattices, hence, universally, appear in any kind of vdW heterostructure, including manually assembled as well as chemical-vapor-deposition-grown [1–4] stacks. In twisted moiré heterostructures, various (unconventional)

superconducting and correlated [5–33], excitonic [34–38], and topological [39–53] phases have been discovered, demonstrating that engineering heterostructures of atomically thin layers of vdW materials opens up a vast space to design properties of quantum materials [54]. However, the atomic layers in vdW materials are not rigid in general, but instead behave as deformable membranes. When two layers with an interfacial defect (i.e., lattice mismatch or twist angle) come in contact, the atomic positions relax to minimize the total energy [55].

Naturally, the relaxation itself is strongest at the defect interface, but we demonstrate here that it may also extend beyond the two atomic layers at the interface. Therefore, the “Lego bricks” analogy put forward by Geim and Grigorieva [56], where heterostructures are composed of mechanically independent layers, though extremely helpful for illustration purposes, needs to be refined considerably to incorporate the flexible nature of each layer as well as the

*These authors contributed equally to this work.

Published by the American Physical Society under the terms of the [Creative Commons Attribution 4.0 International license](https://creativecommons.org/licenses/by/4.0/). Further distribution of this work must maintain attribution to the author(s) and the published article’s title, journal citation, and DOI.

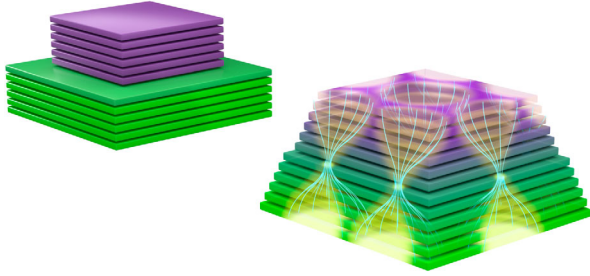


FIG. 1. Two-dimensional heterostructure composed of two mismatched (green and purple) materials. Left panel: Legobricklike illustration in which no atomic relaxation occurs [56]. The two materials have different lattice constants visualized by the width of the stacks. Right panel: illustration including the main finding of this work—layers relax continuously away from the interface. The extent of relaxation is qualitatively encoded in the yellow color. The emergent moiré pattern slowly decays toward the outer layers of the stack.

interplay of mechanical relaxation between different layers. We contrast the two paradigms in Fig. 1, where the left panel illustrates how to understand a stack of two multilayered, mismatched materials in the picture disregarding relaxation. As no relaxation occurs, there is a sharp transition from the bottom stack (green) to the top stack (purple) visualized by the difference in width. In contrast,

a multilayered relaxation leads to a smooth deformation of layers from the bottom to the top (right panel), with signatures of the moiré superlattice slowly decaying away from the interface (yellow vortices).

In fact, we show elaborate domain formation even far away from the interface, stressing the problem is truly three dimensional in nature. From this follows that material properties and the electronic structure [57–60] may be substantially influenced as soon as domain formation occurs, not only in direct vicinity of the interface. Figure 2 summarizes the experimental evidence for the fact that the domain formation picture is rather complex, and for its three-dimensional nature. Figures 2(a)–2(c) explore piezoresponse-force-microscopy (PFM) maps of a terraced few-layer-graphene (FLG) structure on top of a trilayer-graphene (TLG) substrate at a twist angle of 0.66° between the TLG and the FLG part of the stack. PFM is an atomic-force-microscopy (AFM) contact-mode variant which has been shown to be a powerful large-area imaging tool of twisted moiré superlattices [61]. It measures the deflection of the cantilever of a conductive tip at a given point on the sample, due to an oscillating voltage between the metallic tip and a grounded sample (more details in Appendix A). Simplistically, the amplitude of the signal can be interpreted as a measure of local deformation resulted by the electric field, i.e., a local piezoelectric or

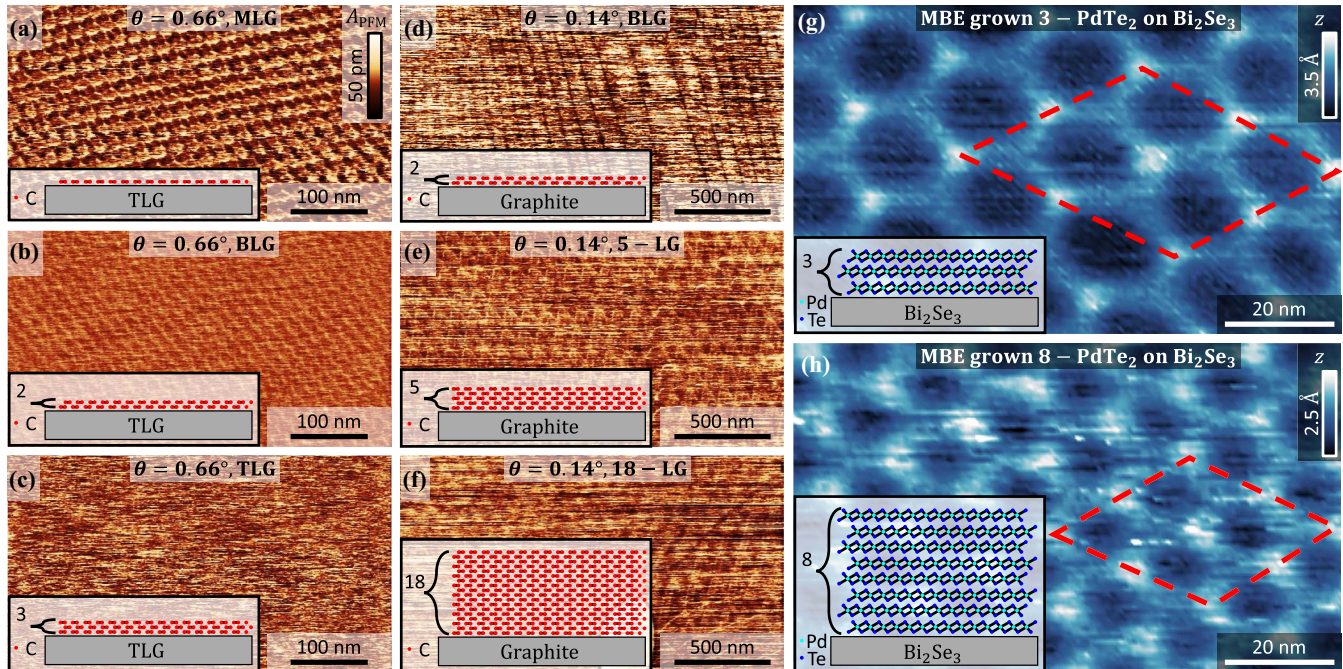


FIG. 2. Experiment motivation: evidence for multilayered relaxation. (a)–(c) PFM amplitude mapping of (a) MLG, (b) BLG, and (c) TLG twisted by 0.65° relative to a TLG substrate. (d)–(f) PFM amplitude mapping of (d) bilayer, (e) five-layered, and (f) 18-layered graphene twisted by 0.14° relative to a graphite substrate. The smaller the twist angle, the thicker the layer through which the moiré superlattice can be resolved. (g), (h) Topography maps by STM of molecular-beam-epitaxy (MBE)-grown PdTe_2 on a Bi_2Se_3 substrate. Two thicknesses are presented, three layers (g) and eight layers (h), showing a thickness dependence of the domain structure and the moiré period indicating a layer-dependent relaxation process. The dashed red diamond marks four moiré unit cells (2×2) in each case. Inset in each panel presents a schematic of the system under study. The experimental details are presented in Appendixes A and B.

flexoelectric effect (see Ref. [61] for a dedicated study of the use of PFM for visualization of moiré superlattices in van der Waals heterostructures). In the context of this work, we consider the PFM contrast as a qualitative measure of the strength of the relaxation at the sample surface. The terraced FLG has monolayer-graphene (MLG), bilayer-graphene (BLG), and TLG segments (highlighted over the optical image in Appendix A), and studied by PFM in Figs. 2(a)–2(c), respectively. As the top-layer thickness increases, the PFM contrast quickly decays. On the other hand, when a similar measurement is performed for a smaller twist angle of 0.14° [Figs. 2(d)–2(f)], the moiré pattern can be visualized by PFM at the surface of a considerably higher stack, even up to 18 atomic layers above the twist interface [Fig. 2(f)]. A different consequence of the layered atomic relaxation emerges in atomically mismatched heterostructures. Such a case is presented in Figs. 2(g) and 2(h) for an epitaxially grown PdTe_2 over a Bi_2Si_3 substrate [62]. In this system, a moiré superlattice emerges from the lattice mismatch between the two materials. Surprisingly, the domain shapes and even the moiré period itself seem to depend on the layer thickness of the PdTe_2 stack. In fact, the observed moiré period exceeds the maximal (zero twist angle) predicted moiré period, solely considering the lattice mismatch. All of the above suggest that the relaxation process and the resulting domain structures are more involved than considered thus far. The spatial extent of the relaxation process and even the moiré period depend on the twist angle and material properties.

In this work, we first develop the multilayered relaxation framework in Sec. II. The framework allows a description of large systems (both in terms of thickness as well as moiré period) which cannot be accessed by atomistic models [63–68]. We then use this framework to reproduce the data in Fig. 2 (cf. Sec. III), explore the three-dimensional nature of the relaxation process (cf. Sec. IV), and study its consequences for the electronic structure using graphitic stacks as a prototypical example in Sec. V.

II. MULTILAYERED RELAXATION: THE APPROACH

In this section, we develop the mathematical framework to allow the description of the atomic relaxation in a multilayered stack of vdW materials. We follow a continuous relaxation approach, conceptually similar to Refs. [69–72]. By continuous relaxation, we assume that the in-plane displacement fields change on a length scale larger than the atomic unit-cell spacing. Using the above assumption for continuous models, the atomic relaxation can be formulated in terms of the energy functional being a sum of a stacking mismatch and an elastic energy term. The sought-after solution is the displacement field that minimizes the total energy. Reference [69] formulated the

problem in configuration space for twisted-bilayer systems. Reference [71] introduced a generalized formalism to potentially treat multiple twisted interfaces, later implemented by Ref. [70] for a specific system of double-twisted-trilayer graphene. In Ref. [72], we solved the problem in real space, thus allowing an omission of the periodicity requirement imposed by the previous treatments in configuration space. It allowed treating experimentally realistic strain-induced-relaxation patterns. The derivation follows the lines and notation of Ref. [72], but instead of treating each flake of the heterostructure as a single elastic membrane, here we assume a stack of m -layered materials labeled by $j \in \{1, 2, \dots, m\}$ with a thickness of n_j layers, respectively, where $j = 1$ denotes the lowermost and $j = m$ the uppermost flake of the heterostructure. Crucially, we allow for individual relaxation in each layer with the in-plane displacement fields of layer k of flake j being described by

$$\mathbf{u}^{(j,k)}(\mathbf{r}) = [u_x^{(j,k)}(x, y), u_y^{(j,k)}(x, y)]^T. \quad (1)$$

The interface between flakes j and $j + 1$ is formed between layer $k = n_j$ of flake j and layer $k = 1$ of flake $j + 1$. The energy functional in our model is composed of the elastic energy density and the stacking energy density,

$$\mathcal{E}(\mathbf{r}, \mathbf{u}, \nabla \mathbf{u}) = \mathcal{E}_{\text{elastic}}(\nabla \mathbf{u}) + \mathcal{E}_{\text{stacking}}(\mathbf{r}, \mathbf{u}). \quad (2)$$

We assume that the $n_1 + n_2 + \dots + n_m$ displacement fields change on a length scale larger than the lattice constants α_j in accordance with prior literature [69,71,72]. However, Ref. [72] was restricted to a single interlayer interface, where now we consider one interface from the twist or lattice constant mismatch between each set of flakes j and $j + 1$, which after relaxation induces $n_j - 1$ interfaces within flake j and similarly $n_{j+1} - 1$ interfaces within flake $j + 1$. We show here that only such a modeling captures the important, finite penetration depth of the relaxation induced by stacking vdW heterostructures from one to a few to a large number of layers in the flakes. To this end, we therefore assume that the stacking energy term can be described by two sets of generalized stacking fault energies (GSFEs): one set covering the initial interfaces between flakes and another set describing the relaxation-induced interfaces within each of the m separate flakes. Note that the separation of the system into a sum over the different interfaces makes a further approximation. It neglects contributions to the stacking energy from neighboring layers beyond the nearest neighbor. Such an approximation would fail to capture subtle differences like the energy imbalance between the Bernal and rhombohedral phases in twisted-double-bilayer graphene [72] and could be relaxed, in principle, in the future.

First, we write the elastic energy density $\mathcal{E}_{\text{elastic}}(\nabla\mathbf{u})$ as a function of the gradients of the displacement fields $\nabla\mathbf{u}$:

$$\mathcal{E}_{\text{elastic}}(\nabla\mathbf{u}) = \sum_{j,1 \leq k \leq n_j} \varepsilon^{(j,k)}(\nabla\mathbf{u}) = \sum_{j,1 \leq k \leq n_j} \left[\frac{K_j(\nabla \cdot \mathbf{u}^{(j,k)})^2}{2} + \frac{G_j}{2} ((\partial_x u_x^{(j,k)} - \partial_y u_y^{(j,k)})^2 + (\partial_x u_y^{(j,k)} + \partial_y u_x^{(j,k)})^2) \right], \quad (3)$$

with $\varepsilon^{(j,k)}(\nabla\mathbf{u})$ the layer-resolved elastic energy density, and K_j and G_j the bulk and shear moduli of flake j , respectively.

The stacking energy density $\mathcal{E}_{\text{stacking}}(\mathbf{r}, \mathbf{u})$ explicitly depends on the position and displacement fields. The general expression is a function of the stacking configuration of each interface. As the stacking configuration is defined in terms of the underlying Bravais lattice, we denote the lattice vectors of flake j with $\alpha_j \mathbf{a}_{1,2}^j$ where $\mathbf{a}_{1,2}^j$ are normalized lattice vectors. Here, we choose the normalization factors α_j to be the lattice constants. For the general case, the relative length of the lattice vectors can be included in $\mathbf{a}_{1,2}^j$, and α_j acts as an overall length scale of flake j . Further, we can always define a two-dimensional matrix A_j that transforms to the lattice vectors such that

$$A_j = [\mathbf{a}_1^j \quad \mathbf{a}_2^j]. \quad (4)$$

We then proceed to define the stacking configuration $\mathbf{\Omega}_0$ of each layer k in flake j as

$$\mathbf{\Omega}_0^{(j,k)}(\mathbf{r}, \mathbf{u}) = \frac{2\pi}{\alpha_j} (A_j)^{-1} [\mathbf{r} - \mathbf{u}^{(j,k)}(\mathbf{r})]. \quad (5)$$

The origins of the unit cells of the layers within the m rigid flakes, respectively, can be chosen at $\mathbf{r}_j = \alpha_j (l \mathbf{a}_1^j + m \mathbf{a}_2^j)$

with integers l and m , such that for zero displacement field $\mathbf{\Omega}_0^{(j,k)}(\mathbf{r}_j, \mathbf{u} = 0) = 2\pi(l, m)^T$.

We assume that each unit area on each interface between two layers contributes to the stacking energy density according to the GSFE for that interface with the relative stacking configuration as input. So, we define the relative stacking configuration $\mathbf{\Omega}_*$ for the intraflake interfaces $k_j = 1, \dots, n_j - 1$ as

$$\mathbf{\Omega}_*^{(j,k_j)} = -\frac{2\pi}{\alpha_j} (A_j)^{-1} (\mathbf{u}^{(j,k_j+1)} - \mathbf{u}^{(j,k_j)}). \quad (6)$$

The relative stacking configuration at the interflake interfaces can similarly be expressed as

$$\mathbf{\Omega}_*^{(j \rightarrow j+1)} = \mathbf{\Omega}_0^{j+1,1} - \mathbf{\Omega}_0^{j,n_j}. \quad (7)$$

As we also want to explicitly treat isotropic expansion of each flake and constant stacking registry shifts of each layer [such as Bernal (*AB*) stacking in graphene], we define the total displacement of flake j and layer k as $\mathbf{U}^{(j,k)} = \mathbf{u}^{(j,k)} + \epsilon_j \mathbf{r}$ with ϵ_j the expansion parameter and add the space-independent constant $\mathbf{\Delta}\mathbf{\Omega}^{(j,k)}$ to the stacking configuration of each layer. These refinements yield the following expressions for the stacking configurations of all interfaces:

$$\mathbf{\Omega}^{(j,k)}(\mathbf{U}) = -\frac{2\pi}{\alpha_j} (A_j)^{-1} (\mathbf{u}^{(j,k_j+1)} - \mathbf{u}^{(j,k_j)}) + \mathbf{\Delta}\mathbf{\Omega}^{(j,k_j+1)} - \mathbf{\Delta}\mathbf{\Omega}^{(j,k_j)}, \quad (8a)$$

$$\mathbf{\Omega}^{(j \rightarrow j+1)}(\mathbf{U}) = \frac{2\pi}{\alpha_{j+1}} (A_{j+1})^{-1} ((1 - \epsilon_{j+1})\mathbf{r} - \mathbf{u}^{(j+1,1)}) - \frac{2\pi}{\alpha_j} (A_j)^{-1} ((1 - \epsilon_j)\mathbf{r} - \mathbf{u}^{(j,n_j)}) + \mathbf{\Delta}\mathbf{\Omega}^{(j+1,1)} - \mathbf{\Delta}\mathbf{\Omega}^{(j,n_j)}. \quad (8b)$$

In general, we formulate the stacking energy density of the system as a function of the relative stacking configurations $\mathbf{\Omega}$:

$$\mathcal{E}_{\text{stacking}}(\mathbf{U}) = \sum_{j=1}^m \sum_{k_j=1}^{n_j-1} V_{\text{GSFE}}^{(j)} \left[\mathbf{\Omega}^{(j,k_j)}(\mathbf{U}) \right] + \sum_{j=1}^{m-1} V_{\text{GSFE}}^{(j \rightarrow j+1)} \left[\mathbf{\Omega}^{(j \rightarrow j+1)}(\mathbf{U}) \right]. \quad (9)$$

For the specific physical systems under consideration in this work, we can use the known form of the GSFE functional [69–72] for each of the interfaces:

$$\begin{aligned} V_{\text{GSFE}}(\mathbf{\Omega}, c_0, \dots, c_5) &= c_0 + c_1 (\cos v + \cos w + \cos(v+w)) + c_2 (\cos(v+2w) + \cos(v-w) + \cos(2v+w)) \\ &+ c_3 (\cos(2v) + \cos(2w) + \cos(2v+2w)) + c_4 (\sin v + \sin w - \sin(v+w)) \\ &+ c_5 (\sin(2v+2w) - \sin(2v) - \sin(2w)), \end{aligned} \quad (10)$$

where we set $(v, w) = \mathbf{\Omega}$ as the components of the relative stacking configurations. The parameters $c_{0,\dots,5}$ depend on the type of interface. As the systems considered in this work consist of $m = 2$ flakes, we need three sets of parameters to calculate the stacking energy density, namely, $c_{0,\dots,5}^{(j)}$ for each of the interfaces within flakes $j = 1, 2$ and $c_{0,\dots,5}^{(1\rightarrow 2)}$ for the interface between flakes 1 and 2 (see Table II for numerical values for the systems under consideration in this work).

To find the solution $\mathbf{u}^{(j,k)}(\mathbf{r})$ and ϵ_j , we minimize the total energy

$$E_{\text{tot}} = \int d^2r (\mathcal{E}_{\text{stacking}}(\mathbf{U}) + \mathcal{E}_{\text{elastic}}(\nabla \mathbf{U})) \quad (11)$$

using standard unconstrained minimization techniques (trust region algorithm). Note that changes to ϵ_j affect the size of the moiré unit cell, so one has to properly account for this effect in defining the grid and the strain terms.

III. MISMATCHED SYSTEM TEST CASE

Motivated by the experimental findings summarized in Figs. 2(g) and 2(h) we consider a PdTe₂/Bi₂Se₃ heterostructure as a specific example of a mismatched heterostructure. The underlying Bravais lattice of both materials is triangular, so we set the lattice vectors as

$$\mathbf{a}_1 = \begin{pmatrix} 1 \\ 0 \end{pmatrix}, \quad \mathbf{a}_2 = \begin{pmatrix} 1/2 \\ \sqrt{3}/2 \end{pmatrix}. \quad (12)$$

The GSFE function parameters $c_{1,\dots,5}$ for each interface of this multilayered PdTe₂ on a Bi₂Se₃ substrate, and the bulk and shear moduli for both materials are taken from density-functional theory (DFT) (see Appendix D). For simplicity, we fix the substrate and allow all PdTe₂ layers to relax individually. We further let the PdTe₂ flake expand isotropically via ϵ_2 . This degree of freedom is crucial in order to explain the observation of Figs. 2(g) and 2(h). Figure 3 summarizes the multilayered relaxation results for different numbers of PdTe₂ layers. Figures 3(a) and 3(b) show how as the layer number drops the relaxation becomes stronger, leading to hexagonal domains and domain expansion. The domain expansion is further quantified in Fig. 3(c) covering the transition between the thick and thin PdTe₂ regimes. It is important to note that all the considered cases show a moiré period λ in excess of the accessible moiré periods, as expected without including the isotropic expansion term [blue shaded region in Fig. 3(c)]. Such an excess moiré period is in agreement with the experimental results. Our results highlight the multilayered trade-off in search of an energy-minimizing solution by the PdTe₂ flake: By conforming to the lattice constant of the Bi₂Se₃ substrate, the stacking energy is reduced at the expense of a penalty of an elastic energy. As the number of layers increases, the elastic

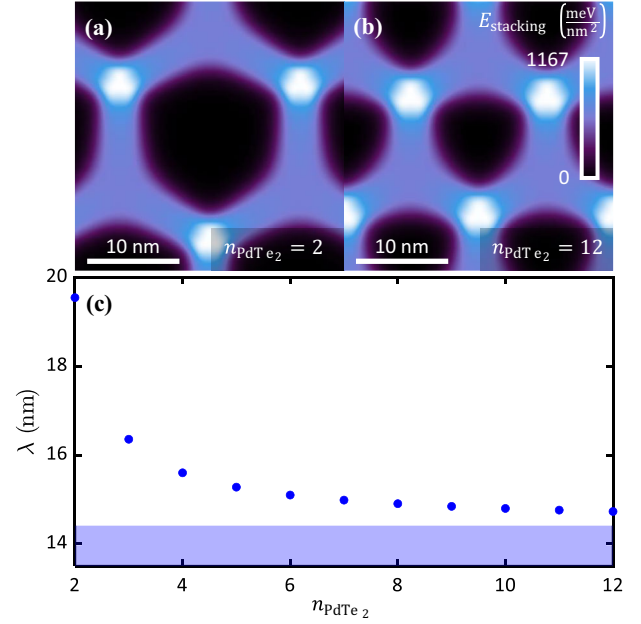


FIG. 3. Modeling of thickness-dependent moiré superlattice in PdTe₂/Bi₂Se₃. (a),(b) Moiré superlattice after mechanical relaxation visualized by the stacking energy density for two (a) and 12 (b) PdTe₂ layers on bulk Bi₂Se₃. (c) Moiré periodicity λ as a function of the number of PdTe₂ layers. The blue region marks the range of accessible moiré period values without isotropic global strain. The relaxation calculations reveal enhanced relaxation and expansion of the moiré periodicity in the thin PdTe₂ layer limit. All considered cases assume no twist between the PdTe₂ and the Bi₂Se₃. See calculation details in Appendix D.

energy term becomes too costly and the relaxation is suppressed. However, at the thin-PdTe₂ limit due to the relative softness of PdTe₂ (see Table II), the elastic energy penalty due to stretching the PdTe₂ is not severe in comparison with the stacking energy benefit, and the result is an enhanced moiré period. Figure 3(c) also highlights the penetration of the relaxation field (here probed by the layer-dependent moiré periodicity λ) induced by the PdTe₂/Bi₂Se₃ interface into the stack which decays exponentially with the number of layers n_{PdTe_2} . To visualize the layer-dependent moiré period, we assemble a video of the pattern in Figs. 3(a) and 3(b) varying n_{PdTe_2} over time [73].

Finally, we note that the layer-dependent moiré wavelength in PdTe₂/Bi₂Se₃ is quantitatively reproduced by our multilayered relaxation framework, considering our data [Figs. 2(g) and 2(h)] as well as the data presented in Ref. [62].

IV. STRUCTURAL STUDY OF A GRAPHENE-BASED SYSTEM

Next, we highlight the impact of employing the multilayered relaxation scheme by the analysis of a graphene-based system compared to the experimental findings

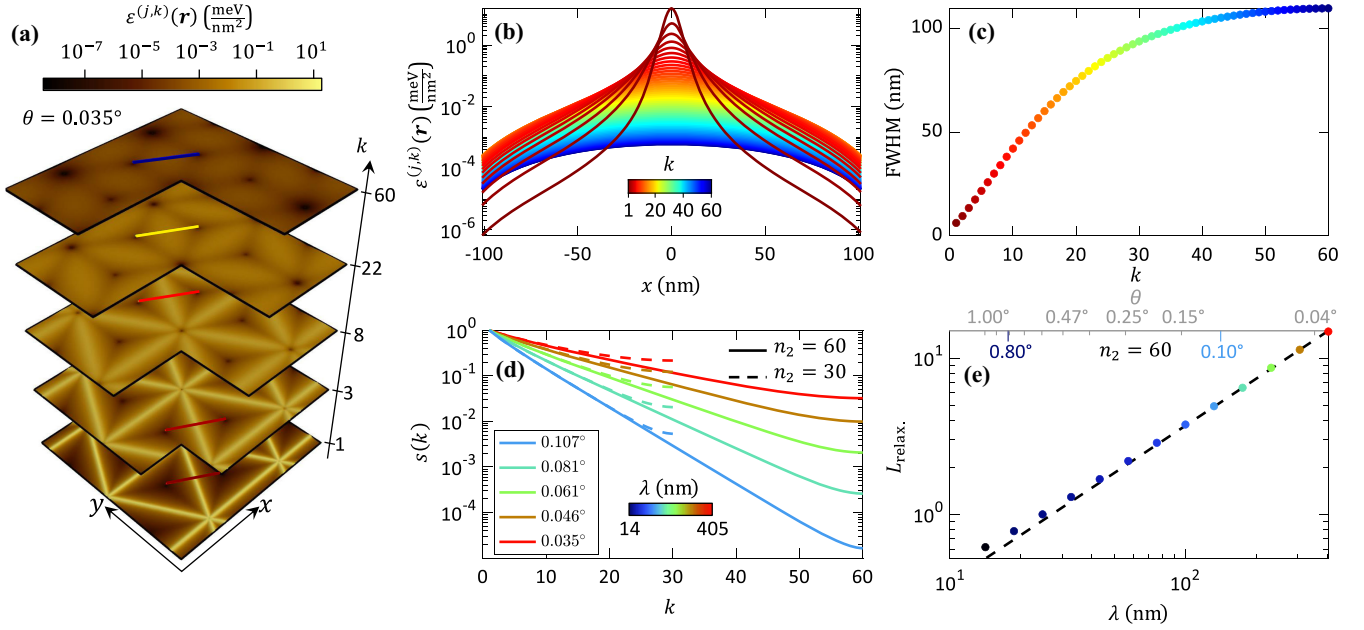


FIG. 4. Multilayered relaxation in twisted-graphite interfaces (a) Elastic energy density in representative layers for an $n_1 = n_2 = 60$ graphite-on-graphite structure with a twist angle $\theta = 0.035^\circ$. (b) Domain-wall profiles and (c) width as full width at half maximum (FWHM) for different layers showing the broadening and weakening of the relaxation away from the interface. Layer number indicated by color bar in (b). (d) Decay of the strength of the relaxation process away from the interface for different twist angles as captured by the displacement field scaling factor (see text for details). Two layer thickness cases are considered. (e) The penetration depth extracted from (d) as a function of the moiré period λ . The penetration depth is shown to be proportional to the moiré period (dashed line).

reported in Figs. 2(a)–2(f). To this end, we study the structural properties of two flakes of Bernal stacked multilayered graphene stacked with a twist at the interface of the two flakes. As in the previous section, the Bravais lattice of graphene is also triangular. However, we need to implement the twist angle θ as a two-dimensional rotation matrix in the transformation from flake 1 to 2: $A_2 = R(\theta)A_1$. Moreover, the GSFE parameters and shear and bulk moduli of graphene are presented in Appendix D.

As a primary result, we obtain the layer- and space-resolved elastic energy density $\varepsilon^{(j,k)}(\mathbf{r})$. This can be viewed as a layer-resolved elastic energy tomograph scanning through the height of the stacks. Figure 4(a) displays this result for a small twist angle system ($\theta = 0.035^\circ$) and $n_1 = n_2 = 60$. The layer-resolved elastic energy tomograph emphasizes two main points: First, the relaxation pattern decays exponentially as a function of the distance to the interface. Second, the system forms triangular relaxation domains separated by domain walls connecting the AB and BA regions of the interfacial moiré pattern. In Fig. 4(b), we plot the elastic energy density along the line cut across a domain wall [as indicated in the tomograph of Fig. 4(a)] for all layers. At the interface, these domains have very sharp domain walls. The width of the domain wall grows as the distance to the interface increases, while at the same time its height declines. In Fig. 4(c), we quantify this behavior by plotting the FWHM as a function of the

layer index k . We color code the value of k consistently across Figs. 4(a)–4(c).

Upon varying twist angle, we can examine how the relaxation behavior evolves. To this end, we analyze the scaling of the atomic displacements $\mathbf{u}^{(j,k)}(\mathbf{r})$ as a function of k in the second flake $j = 2$. To do so, we quantify the strength of the relaxation in layer k of flake 2 by defining a layer-dependent scaling factor $s(k)$ which is chosen such that the in-plane integrated squared difference

$$D(k) = \int d^2r \|\mathbf{u}^{(2,1)}(\mathbf{r}) - s(k)\mathbf{u}^{(2,k)}(\mathbf{r})\|^2 \quad (13)$$

of displacement fields of the k th layer $\mathbf{u}^{(2,k)}(\mathbf{r})$ and the first layer $\mathbf{u}^{(2,1)}(\mathbf{r})$ is minimal.

Figure 4(d) shows the scaling factor $s(k)$ for five twist angles $0.035^\circ \leq \theta \leq 0.107^\circ$, with red curves corresponding to the small twist angle (large moiré wavelength λ) case and blue curves to the large twist angle (small λ) case. For each of the twist angles considered, we additionally set the number of layers of the second flake to $n_2 = 30$ (dashed lines) and $n_2 = 60$ (solid lines). Up to a cutoff when approaching the upper end of the stack (dependent on the height n_2), we find penetration of the relaxation fields into the stack which decays exponentially. The exponent decreases with the twist angle, yielding longer-ranged relaxation effects for smaller twist angle. We quantify

the exponential decay of the relaxation effects by determining the penetration depth L_{relax} of the relaxation pattern. Here, we define L_{relax} through

$$s(k) \approx e^{-k/L_{\text{relax}}}, \quad (14)$$

and calculate it using a fit for the case $n_2 = 60$ as a function of λ . The result is shown in Fig. 4(e) with consistent color coding of λ and θ across Figs. 4(d) and 4(e). We observe that the penetration depth $L_{\text{relax}}(\lambda)$ scales linearly with λ in the small- θ and large- n_2 limit.

For the two angles observed in the experiment [Figs. 2(a)–2(f)], we thus expect a penetration depth that is $0.66^\circ/0.15^\circ \approx 4.7$ times as large in the 0.15° system than in the 0.66° system. As the 0.66° case cannot be assumed to be in the large- n_2 limit ($n_2 = 3$), we conclude that the theory qualitatively agrees with the experimental data—18 layers/3 layers is the same order of magnitude as 4.7.

V. MULTILAYERED RELAXATION'S IMPACT ON THE ELECTRONIC STRUCTURE OF A GRAPHITIC SYSTEM

As suggested by our experimental data and confirmed by using the multilayered relaxation framework, the in-plane relaxation can affect layers far from the interface of the flakes. For twisted graphitic systems, this becomes particularly prominent at small twist angle (cf. Figs. 2 and 4). Such in-plane relaxations generate effective magnetic fields [74–77] and therefore may have a substantial impact on the electronic structure. Furthermore, using relaxed atomic positions has been shown to be crucial to explain low-energy properties of twisted graphitic systems [57–59,78,79]. Therefore, we analyze the effect of multilayered relaxation on the electronic structure of twisted many-layer graphene systems in the following.

We focus on the case of several layers of Bernal stacked graphene on bulk graphite (corresponding to the small-angle experimental PFM data shown in Fig. 2). We approximate the bulk by $n_1 = 20$ graphene layers and vary the number of layers in the top (twisted) flake from $n_2 = 3$ to $n_2 = 20$. We set the twist angle to $\theta = 0.1^\circ$ (the $\theta = 0.8^\circ$ case can be found in Appendix F) which implies a unit cell of approximately 150 nm in size and approximately 650 000 carbon atoms per layer. For a multilayer geometry, the number of atoms is intractable for a tight-binding framework, and so we adopt the Bistritzer-MacDonald continuum model of twisted-bilayer graphene [80–84] to include arbitrary in-plane relaxations (see Refs. [85,86]) and Bernal multilayer hopping terms [65,87–89].

For our analysis, we make use of the Bistritzer-MacDonald Hamiltonian, which can be viewed as a reciprocal moiré lattice vector expansion of the full tight-binding Hamiltonian of the system. The expansion as presented below is valid for SE-odd moiré structures [81], which applies to the graphitic systems studied in this work. With

$\mathbf{B}_{1,2}$ the reciprocal moiré lattice vectors, we expect the multilayered Hamiltonian to be a matrix in the “indices” $\mathbf{G} = p\mathbf{B}_1 + q\mathbf{B}_2$, $p, q \in \mathbb{Z}$. The expansion is then truncated at $\|\mathbf{G}\| < G_c$, where G_c must be chosen large enough to ensure convergence. We further need to account for the sublattice (A, B), flake, layer, and valley $\xi = \pm 1$ degrees of freedom. For the sake of clarity of notation, we drop flake indices and continuously index the layers with $l = 1, \dots, n_1 + n_2$, where $l \leq n_1$ corresponds to flake $j = 1$ and $l > n_1$ to flake $j = 2$.

Our starting point is the intralayer continuum Hamiltonian, which is composed of the following three parts:

$$H_{\text{intra}}^{GG',\xi,l}(\mathbf{k}) = H_{\text{Bernal}}^{G,\xi,l}(\mathbf{k})\delta_{G,G'} + H_{\text{mag}}^{GG',\xi,l} + H_{\text{stat}}^{GG',\xi,l}. \quad (15)$$

Only the standard Bernal intralayer Hamiltonian explicitly depends on momentum \mathbf{k} (in the moiré Brillouin zone). As the low-energy states all are close to the individual graphene layers' K_ξ -points, we shift and rotate the momentum vector:

$$\mathbf{K}_v = R(\theta^l)(\mathbf{k} - \mathbf{K}_\xi^l + \mathbf{G}), \quad (16)$$

with $R(\theta^{l>n_1}) = R(\theta)$ for the twisted layers in flake 2 and $R(\theta^{l \leq n_1}) = \mathbb{1}$ for the nontwisted layers in flake 1. The K_ξ -points of a given layer can be expressed by the reciprocal moiré lattice vectors as

$$\mathbf{K}_\xi^{l \leq n_1} = -\xi/3(2\mathbf{B}_2 + \mathbf{B}_1), \quad (17)$$

$$\mathbf{K}_\xi^{l > n_1} = -\xi/3(\mathbf{B}_2 - \mathbf{B}_1). \quad (18)$$

Using $\mathbf{K}_v = \xi\mathbf{K}_{v,x} + i\mathbf{K}_{v,y}$, the Bernal intralayer Hamiltonian as a matrix in (A,B) sublattice space is then expressed as

$$H_{\text{Bernal}}^{G,\xi,l}(\mathbf{k}) = \begin{pmatrix} \delta_{p,A} + \delta_{\text{isp}}^l & -v_F \mathbf{K}_v^* \\ -v_F \mathbf{K}_v & \delta_{p,B} + \delta_{\text{isp}}^l \end{pmatrix}. \quad (19)$$

Here, v_F denotes the Fermi velocity of graphene. We further include the intrinsic symmetric polarization δ_{isp}^l that is non-zero only in the central (twisted) layers: $\delta_{\text{isp}}^{n_1} = \delta_{\text{isp}}^{n_1+1} = \delta_{\text{isp}}$. Additionally, we account for sublattice polarization with $\delta_{p,A} = \delta_p$, $\delta_{p,B} = 0$ in all layers.

The other two parts of the intralayer continuum Hamiltonian Eq. (15) depend on the in-plane displacement field. As the in-plane displacement field is periodic in moiré lattice vectors and varies within the moiré unit cell, we apply a Fourier transform and obtain a representation in reciprocal moiré lattice vector space:

$$\mathbf{u}_G^l = \sum_{\mathbf{r}} e^{-i\mathbf{G}\cdot\mathbf{r}} \mathbf{u}^{l=(j,k)}(\mathbf{r}). \quad (20)$$

First, we can write down the vector potential of the effective magnetic field generated by the displacement field as a function of \mathbf{G} :

$$\mathbf{A}^{G,l} = \begin{pmatrix} iG_x & -iG_y \\ -iG_y & -iG_x \end{pmatrix} \cdot \mathbf{u}_G^l. \quad (21)$$

This potential is added to the Hamiltonian with a coupling strength g_2 by standard substitution:

$$H_{\text{mag}}^{GG',\xi,l} = g_2[\sigma_x A_x^{G-G',l} + \xi \sigma_y A_y^{G-G',l}], \quad (22)$$

with σ_x and σ_y Pauli matrices in sublattice space. Note that the initial dependence of the displacement field on the position vector \mathbf{r} is translated to a (reciprocal moiré lattice) momentum transfer $\mathbf{G} - \mathbf{G}'$.

Second, the displacement field also generates a static potential that leads to the following contribution to the intralayer Hamiltonian:

$$H_{\text{stat}}^{GG',\xi,l} = i \eta g_1 [(\mathbf{G} - \mathbf{G}') \cdot \mathbf{u}_{\mathbf{G}-\mathbf{G}'}^l]. \quad (23)$$

Here, g_1 is the static potential's coupling strength.

The intralayer Hamiltonian is accompanied by several interlayer coupling terms. For all nontwisted interfaces, we employ an effective graphite Hamiltonian. Its coupling from one to the next layer reads [as a matrix in $(A_l B_l; A_{l+1} B_{l+1})$ sublattice space] [65,89]

$$H_{\text{inter}}^{GG',\xi,l,l+1}(\mathbf{k}) = \begin{pmatrix} \gamma_4 K_v^* & \gamma_1 \\ \gamma_3 K_v^* & \gamma_4 K_v \end{pmatrix} \delta_{\mathbf{G},\mathbf{G}'}. \quad (24)$$

The coupling to second-next layers is taken into account as shown in Ref. [87] and reads as a matrix in $(A_l B_l; A_{l+2} B_{l+2})$:

$$H_{\text{inter}}^{GG',\xi,l,l+2}(\mathbf{k}) = \begin{pmatrix} \gamma_5 & 0 \\ 0 & \gamma_2 \end{pmatrix} \delta_{\mathbf{G},\mathbf{G}'}. \quad (25)$$

For the values of the hopping parameters $\gamma_{1,\dots,5}$ see Table I.

The interlayer Hamiltonian of the twisted interface between layers $l = n_1$ and $l = n_1 + 1$ encodes the interfacial moiré pattern and is therefore a matrix in \mathbf{G} . The

TABLE I. Parameters for setup of the multilayered continuum Hamiltonian. The length of the graphene lattice vectors $\mathbf{a}_{1,2}$ and the lattice constant a is needed for proper normalization of several hopping parameters.

$a = \alpha \ \mathbf{a}_1\ = \alpha \ \mathbf{a}_2\ $	$t_0 = 0.0797 \text{ eV}$
$\gamma_1 = 0.3513 \text{ eV}$	$\gamma_2 = -0.0105 \text{ eV}$
$\gamma_3 = 0.2973 \text{ eV} \times a \times \sqrt{3}/2$	$\gamma_4 = 0.1954 \text{ eV} \times a \times \sqrt{3}/2$
$\gamma_5 = 0.0187 \text{ eV}$	$\delta_p = 0.0540 \text{ eV}$
$\delta_{\text{isp}} = -0.03 \text{ eV}$	$g_2 = -6.3585 \text{ eV}$
$g_1 = 4.0 \text{ eV}$	$v_F = 2.1354 \text{ eV} \times a$

coupling function U^ξ depends on the difference of in-plane displacement and is most easily formulated in real space:

$$U^\xi(\mathbf{r}) = - \sum_{j=1}^3 M_j^\xi t_0 \exp[i\mathbf{Q}_j^\xi \cdot (\mathbf{u}^{(1,n_1)}(\mathbf{r}) - \mathbf{u}^{(2,1)}(\mathbf{r})) + i\delta \mathbf{k}_j \cdot \mathbf{r}]. \quad (26)$$

Here, t_0 is the out-of plane hopping and M_j^ξ are matrices in sublattice $(A_{n_1}, B_{n_1}; A_{n_1+1}, B_{n_1+1})$ space:

$$M_1^\xi = \begin{pmatrix} 1 & c \\ c & 1 \end{pmatrix}, \quad M_2^\xi = \begin{pmatrix} 1 & cw^{-\xi} \\ cw^\xi & 1 \end{pmatrix}, \quad M_3^\xi = (M_2^\xi)^*, \quad (27)$$

with $c = 1.22333$ the ratio of the AB -stacking to AA -stacking interlayer tunneling due to out-of plane corrugations and $w = \exp(2\pi i/3)$. The unperturbed momentum-transfer vectors $\delta \mathbf{k}_j$ read

$$\delta \mathbf{k}_1 = 0, \quad \delta \mathbf{k}_2 = \xi \mathbf{B}_1, \quad \delta \mathbf{k}_3 = \xi(\mathbf{B}_1 + \mathbf{B}_2), \quad (28)$$

and the displacement-induced momentum-transfer vectors \mathbf{Q}_j^ξ are the center of the twisted and nontwisted K_ξ -points of the original graphene lattices:

$$\mathbf{Q}_j^\xi = R(2\pi/3j)[\mathbf{K}_\xi^0 + \tilde{\mathbf{K}}_\xi^0]/2, \quad (29)$$

$$\mathbf{K}_{+1}^0 = -1/3(2\mathbf{b}_1 + \mathbf{b}_2), \quad \mathbf{K}_{-1}^0 = R(2\pi/6)\mathbf{K}_{+1}^0, \quad (30)$$

$$\tilde{\mathbf{K}}_{+1}^0 = -1/3(2\tilde{\mathbf{b}}_1 + \tilde{\mathbf{b}}_2), \quad \tilde{\mathbf{K}}_{-1}^0 = R(2\pi/6)\tilde{\mathbf{K}}_{+1}^0, \quad (31)$$

where $\mathbf{b}_{1,2}$ ($\tilde{\mathbf{b}}_{1,2}$) denote the reciprocal lattice vectors of the nontwisted- (twisted-) graphene lattice. To arrive at a consistent description, we further take the Fourier transform of the real-space interlayer tunneling $U^\xi(\mathbf{r})$ and obtain a coupling function $U^{GG',\xi}$.

The full single-particle continuum Hamiltonian for valley ξ follows as

$$H_\xi^{GG',ll'}(\mathbf{k}) = H_{\text{intra}}^{GG',\xi,l}(\mathbf{k})\delta_{l,l'} + H_{\text{inter}}^{GG',\xi,ll'}(\mathbf{k})\delta_{\text{bulk}}^{ll'} + U^{GG'}\delta_{\text{twist}}^{ll'}, \quad (32)$$

where $\delta_{\text{bulk}}^{ll'} = 1$ for l and l' in the same flake and $\delta_{\text{twist}}^{ll'} = 1$ for l and l' corresponding to the twisted interface coupling ($l = n_1$ to $l' = n_1 + 1$). For all other combinations of layers, these ‘‘delta functions’’ are zero. As the full Hamiltonian requires several numerical parameters, we provide an overview of their values in Table I.

The application of the continuum description Eq. (32) to the $\theta = 0.1^\circ$ twisted many-layer graphene-on-graphite system is presented in the following. We inspect the local spectral density in the top layer of the twisted flake as an

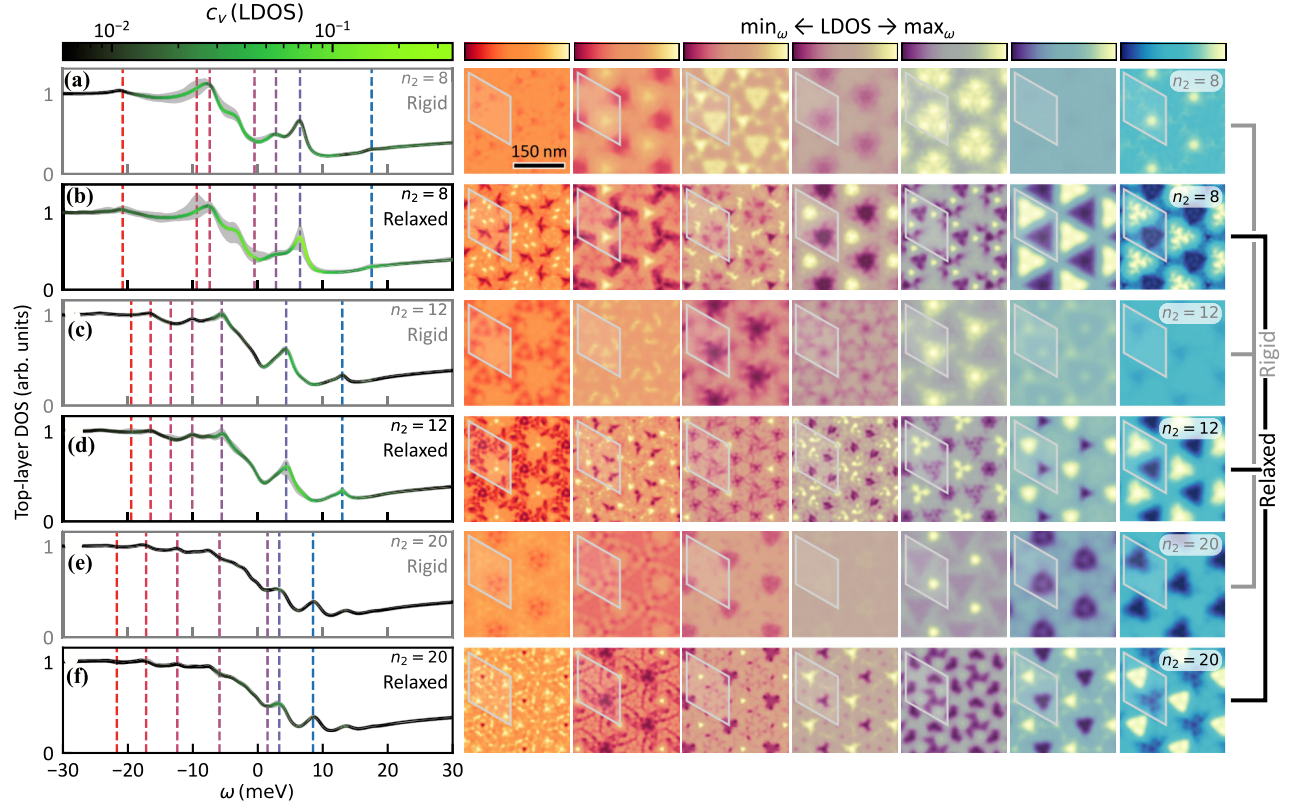


FIG. 5. Electronic structure properties for graphite on graphite at twist angle of $\theta = 0.1^\circ$. Each row (a)–(f) corresponds to the same system where we vary the number of graphene layers in the top flake (n_2) and relaxed or rigid atomic structures across rows. Left subpanels: frequency (ω) resolved DOS of the outermost layer of the top graphite flake. Panels (a),(c),(e) represent simulations using rigid structures, and panels (b),(d),(f) relaxed structures. The number of layers of the bottom flake is fixed at $n_1 = 20$. We color code the coefficient of variation ($c_v = \sigma/\mu$) of the LDOS in the top layer as a function of ω . Light green indicates strong spatial variations in the top-layer LDOS, whereas black corresponds to a uniform LDOS. The gray area in the background of the curves indicates the minimum and maximum values of the LDOS at a given frequency. The frequencies are indicated in the left subpanels as dashed, colored vertical lines varying from red (low frequencies) to blue (high frequencies). The color maps for the LDOS maps are chosen to be consistent with this coloring. Light (yellow) regions correspond to high intensity and dark (red \rightarrow blue) regions to low intensity. For each configuration, the rigid (gray) and relaxed (black) panels in two subsequent rows share a color scale to make differences visible. The system’s unit cell is indicated in each of the small subpanels. All plots on the right-hand side share the scale bar plotted in the top left subpanel.

observable experimentally accessible by scanning tunneling microscopy. To isolate the effect of the relaxation, we compare the rigid system [where $\mathbf{u}^{(j,k)}(\mathbf{r}) \equiv 0$] to the relaxed one where we apply the method of Sec. II to find $\mathbf{u}^{(j,k)}(\mathbf{r})$.

The left subpanels in Fig. 5 present the integrated (over space) top-layer density of states (DOS) as a function of the energy ω . Over Figs. 5(a)–5(f), the top flake layer number n_2 is varied from $n_2 = 8$ to $n_2 = 20$ (the $n_2 = 3$ to $n_2 = 6$ cases are shown in Appendix F). We subdivide the rigid [Figs. 5(a), 5(c), and 5(e)] and the relaxed [Figs. 5(b), 5(d), and 5(f)] cases. To highlight the spatial variations, we color the curves with the coefficient of variation of the top-layer LDOS (over space) that is defined as

$$c_v(l, \omega) = \frac{\text{std}_{\mathbf{r}}(\text{LDOS}(l, \omega, \mathbf{r}))}{\text{mean}_{\mathbf{r}}(\text{LDOS}(l, \omega, \mathbf{r}))}. \quad (33)$$

Additionally, we add a gray background that corresponds to the minimum and maximum values taken by the LDOS of the outermost layer. By the DOS and its spatial variations, we can identify regions in ω (for each n_2) where the effect of relaxation is most pronounced. We highlight these regions by vertical dashed lines colored from red to blue. The right subpanels in each row Figs. 5(a)–5(f) show the corresponding spatial map of the outermost layer LDOS for these specific ω and n_2 values. Note that two subsequent rows [e.g., Figs. 5(a) and 5(b)] share a color map for each ω and n_2 such that the differences from the relaxed to the rigid case become visible. The color maps of the LDOS maps are chosen to correspond to the colors indicating ω in the DOS plot on the left. We provide the LDOS maps for all frequencies as videos in the Supplemental Material [73]. For $n_2 = 8$ and $n_2 = 12$, the LDOS maps for rigid atomic structures Figs. 5(a) and 5(c) clearly show less variation

than the ones for relaxed atomic structures Figs. 5(b) and 5(d) for all values of ω chosen. Likewise, the c_v value is much larger over a substantial range of frequencies [see left subpanels for Figs. 5(a)–5(d)]. The local density of states shows strong differences between the rigid and relaxed calculations in these cases. At a twist angle of $\theta = 0.1^\circ$, this difference highlights the relevance of relaxation effects for a description of the electronic properties. At $n_2 = 20$, over a broad range of frequencies the value of c_v is minor in both the relaxed Fig. 5(f) and rigid Fig. 5(e) cases. Only at around $\omega \approx 3$ meV there is a slightly more pronounced spatial variation showing that for the twist angle of $\theta = 0.1^\circ$ the effects of relaxation do not penetrate through $n_2 = 20$ layers in accord with the analysis of $s(k)$ above suggesting $L_{\text{relax}} \sim 5$ layers.

VI. OUTLOOK

Our work highlights the effects of multilayered relaxation in various vdW heterostructures. We show experimentally using PFM that for multilayered-graphene stacks with a twisted interface, the atomic displacement can propagate deep into the flake for small twist angles [see Figs. 2(a)–2(f)]. We complement this experimental observation of the relevance of relaxation in twisted vdW heterostructures with an untwisted mismatched system: multilayered PdTe₂ on a Bi₂Se₃ substrate. In this system, multilayered relaxation is of great importance as well, and it becomes distinctively visible as a change in lattice constant as the number of PdTe₂ layers is increased [cf. Figs. 2(g) and 2(h)]. We thus establish that multilayered relaxation is highly relevant for the engineering of stacked vdW heterostructures in the twisted and nontwisted context. On the one hand, this emphasizes the need of a deepened understanding of relaxation and a refinement of the Lego-like picture often employed in the field [56]. On the other hand, it adds yet another tuning knob to the thriving field of vdW heterostructure engineering. As exemplified here for PdTe₂ on a Bi₂Se₃ substrate, the effective lattice constant can be tuned over a rather versatile range by multilayered relaxation effects.

In tandem, we develop a machinery that allows us to simulate and understand these relaxation properties given the generalized stacking fault energy functional from *ab initio* calculations. Within this approach, we treat each layer of the heterostructure stack as a separate membrane. Our simulations fully support the experimental evidence of three-dimensional, layered relaxation patterns in both systems: First, we reproduce the stacking-height-dependent lattice constant evolution in a stack of PdTe₂ on Bi₂Se₃ (Fig. 3). Second, we observe that the penetration depth of relaxation domains in twisted-graphite stacks linearly increases with moiré wavelength (Fig. 4). These two examples emphasize how the three-dimensional nature of multilayered heterostructures needs to be taken into account when modeling their atomic structure.

Ultimately we predict differences in electronic properties arising from the atomic relaxation in multilayered graphene

twisted on graphite. Similar to the notion of penetration depth of the relaxation pattern, we see that the local density of states in the outermost layer of the graphene stack sensitively depends on whether the atomic positions of the crystal are relaxed or not. For a small twist angle ($\theta = 0.1^\circ$), we demonstrate that the local variation of the electron density in the outermost graphene layer is much stronger when the multilayered relaxation pattern is taken into account properly (Fig. 5). We propose to analyze such a multilayered (small-angle) twisted graphene-on-graphite stacks using scanning tunneling microscopy in the future, as the local electronic density as a function of the frequency can be used to probe the here-predicted effects of relaxation on the electronic structure in precise manner. The strong effects of relaxation on the electronic properties of the stack highlight that also these properties, including their collective behavior, can be engineered by the relaxation of a stacked vdW heterostructure even beyond the few-layer paradigm.

ACKNOWLEDGMENTS

Nanoimaging research at Columbia is supported by DOE-BES Grant No. DE-SC0018426. Research at Columbia on moiré superlattices is entirely supported as part of Programmable Quantum Materials, an Energy Frontier Research Center funded by the U.S. Department of Energy (DOE), Office of Science, Basic Energy Sciences (BES), under Award No. DE-SC0019443. Research on atomic relaxation is supported by Grant No. W911NF2120147. We acknowledge funding by the Deutsche Forschungsgemeinschaft (DFG, German Research Foundation) under RTG 1995 and RTG 2247, within the Priority Program SPP 2244 “2DMP,” under Germany’s Excellence Strategy—Cluster of Excellence Matter and Light for Quantum Computing Grant No. EXC 2004/1–390534769 and—Cluster of Excellence and Advanced Imaging of Matter Grant No. EXC 2056–390715994. We acknowledge computational resources provided by the Max Planck Computing and Data Facility and RWTH Aachen University under Project No. rwth0716. This work was supported by the Max Planck–New York City Center for Nonequilibrium Quantum Phenomena. D. N. B. is a Moore Investigator in Quantum Materials EPIQS GBMF9455. D. H. was supported by a grant from the Simons Foundation (Grant No. 579913). We thank Oxford Instruments Asylum Research for performing the large-scale tapping mode scan presented in Appendix A (Fig. 7).

D. H. and L. K. contributed equally to this work.

APPENDIX A: GRAPHENE EXPERIMENT

Using an optical microscope, we identify exfoliated graphene flakes with tiered graphene thicknesses in close proximity to a bulk graphite flake from the same crystal. Samples are then assembled using a dry transfer technique using a slide with polycarbonate film on top of a

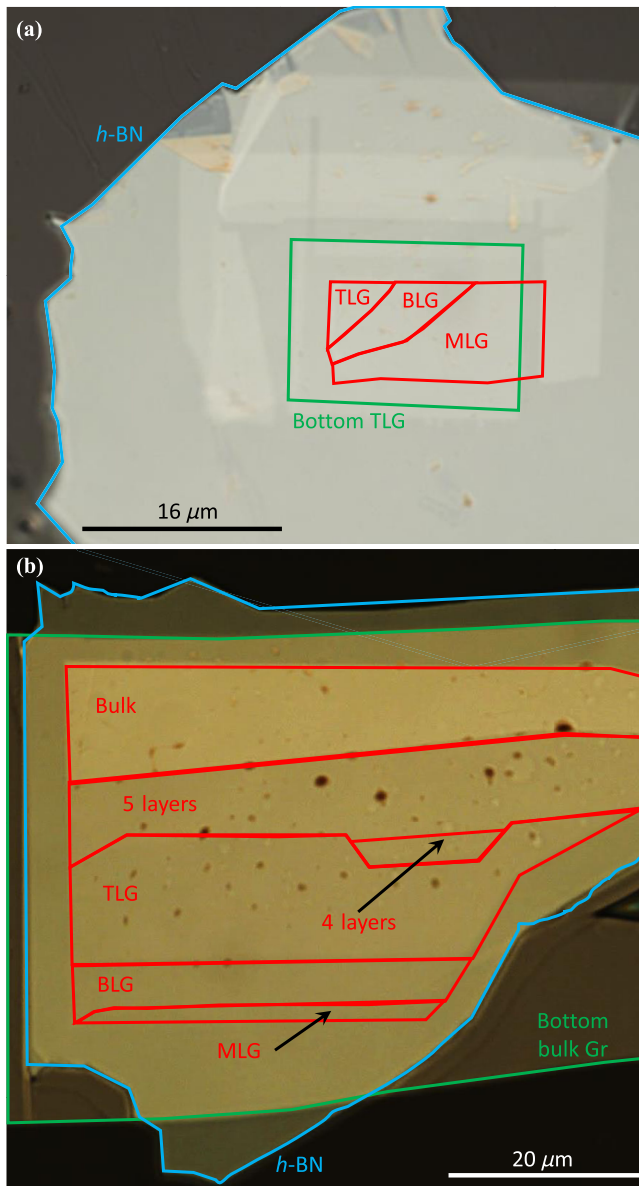


FIG. 6. Optical images of the studied terraced graphene samples. (a) The sample measured in Figs. 2(a)–2(c) (twist angle of approximately 0.66°) with *h*-BN, bottom trilayer graphene, and top mono-, bi- and trilayer graphene regions indicated by blue, green, and red contours, respectively. (b) The sample measured in Figs. 2(d)–2(f) (twist angle of approximately 0.1°) with regions indicated by similar colors. The top layer has bulk (estimated to be 18 layers), five layers, four layers, TLG, BLG, and MLG regions as indicated.

polydimethyl siloxane dome [90]. We use the slide to first pick up a BN flake of thickness 30–40 nm, which is then placed into contact with the bulk graphite flake. After picking up the bulk graphite, we then rotationally misalign the transfer stage by a small angle of less than 1° before picking up the tiered graphene flake. The completed heterostructure remains on the polymer stamp slide during subsequent experimental measurements. Figure 6 presents

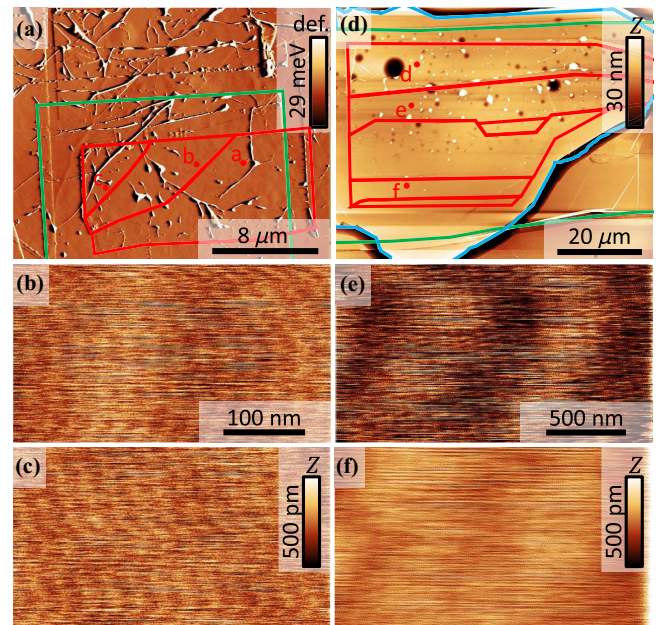


FIG. 7. Topography maps of the studied terraced graphene samples. (a) Topography map of the sample measured in Figs. 2(a)–2(c), as reflected by the deflection error channel in contact mode. The layer markings are as in Fig. 6(a). (b),(c) Topography maps in contact mode taken simultaneously with Figs. 2(a) and 2(b), respectively [(b),(c) share a color scheme and a scale bar]. (d) Topography map of the sample measured in Figs. 2(d)–2(f), as reflected by tapping mode scan. The layer markings are as in Fig. 6(b). (e),(f) Topography maps in contact mode taken simultaneously with Figs. 2(d) and 2(e), respectively [(e),(f) share a color scheme and a scale bar]. The locations of the scans of Figs. 2(a)–2(f) are marked over (a) and (b).

optical images of the completed heterostructures studied in Fig. 2. Topography data of these samples are shown in Fig. 7. While the large-scale topography maps of Figs. 7(a) and 7(d) indicate the existence of bubbles and wrinkles in the structures, the samples have an abundance of flat regions that are meticulously studied. Fig. 7(a) is acquired with a Bruker Dimension Icon with a Nanoscope V Controller, and Fig. 7(d) is acquired by a Jupiter XR AFM by Oxford Instruments Asylum Research. We use piezoresponse force microscopy (PFM) to image the moiré superlattice between the rotationally misaligned tiered graphene flake and the bulk graphite [61]. In PFM, we apply an ac bias between the conductive probe and the microscope stage (on which the sample is directly mounted, giving an approximate distance of about $500\ \mu\text{m}$ between biased tip and ground), which induces a periodic deformation of the sample through the piezoelectric effect. Even though the sample is not contacted, and thus one may raise the concern of its potential being ill-defined, empirically the results of PFM studies do not seem to be sensitive to the sample being properly grounded. Apparently, due to the proximity to a grounded plane, the stage still provides a good dc reference for the oscillating fast perturbations made by the metallic tip (at hundreds of kHz). The

phase and amplitude of the local deformation provide the strongest contrast to visualize moiré in our samples. ac bias magnitudes are 500–1000 mV with resonance frequencies in the range of 270–300 kHz for vertical and 750–850 kHz for lateral PFM. The experiments are performed in a Bruker Dimension Icon with a Nanoscope V Controller, using Oxford Instrument Asylum Research ASYELEC-01 Ti/Ir-coated silicon probes. While the PFM signal is commonly interpreted as a measure of local deformation resulting from the electric field exerted by the tip, i.e., a local piezoelectric or flexoelectric effect (see Ref. [61]), the exact physical mechanism responsible for the contrast is not necessarily purely of such origin. When looking at the contact-mode scans of Figs. 7(b), 7(c), 7(e), and 7(f) taken simultaneously with those of Figs. 2(a), 2(b), 2(d), and 2(e), respectively, one may notice faint periodic structure, which may reflect some topographic features of the moiré lattice. Regardless of the exact mechanism for the PFM contrast, we consider it to be correlated with the strength of the relaxation at the sample surface.

The PFM scans of 20 different locations in the approximately 0.66° sample reveals twist angles ranging from 0.63° to 0.8° based upon the moiré wavelength. For the approximately 0.1° sample, we take scans in 48 different locations, showing a rather uniform twist angle of $0.11^\circ \pm 0.02^\circ$ through the two to five top-layer graphene and bulk top-layer graphene regions. In both samples, the thinner top-layer regions (MLG and to some extent the BLG as well) are more susceptible to strain, as indicated by the moiré superlattice.

One may wonder whether the observed moiré patterns may actually originate from a hexagonal boron nitride (*h*-BN)-graphene moiré interface. For the case of the single-, bi-, and trilayer graphene twisted at an angle of 0.66° [cf. Figs. 2(a)–2(c)], we note that we can exclude a potential moiré lattice formed by aligned *h*-BN and the bottom multilayered graphene as a source of PFM contrast due to the different length scales involved. At maximum, *h*-BN and graphene form a moiré lattice with $\lambda_{h\text{-BN}}^{\max} \approx 14$ nm [91], whereas the moiré wavelength observed experimentally is $\lambda_{\text{graphene}} = a_{\text{graphene}} / [2 \sin(\theta/2)] \approx 18\text{--}22$ nm, which is significantly larger than 14 nm and therefore corresponds to the mentioned graphene-graphene moiré lattice with twist angle of $\theta = 0.66^\circ$.

APPENDIX B: PdTe₂/Bi₂Se₃ EXPERIMENT

The PdTe₂ thin films are grown on a Bi₂Se₃ substrate in an integrated MBE-STM ultrahigh-vacuum system with base pressure below 2×10^{-10} mbar. The Bi₂Se₃ is prepared by *in situ* cleaving the surface and subsequent annealing to 250 °C for one hour to degas. Then, high-purity Pd (99.95%) and Te (99.9999%) are evaporated from an electron-beam evaporator and a standard Knudsen cell, respectively, with a flux ratio of 1 : 10. The deposition rate of Pd and Te atoms is monitored by a quartz oscillator. The temperature of the substrate is kept at 210 °C during the growth.

After the initial annealing of the Bi₂Se₃, the substrate is transferred *in situ* to the Aarhus STM stage with a tungsten tip. STM measurements are taken of the substrate to ensure the quality of the substrate. Once deposition of the Pd and Te is complete, the sample is transferred *in situ* to the STM stage for surface topography mapping.

APPENDIX C: JUSTIFYING ASSUMPTIONS OF IN-PLANE RELAXATION MODEL: ESTIMATING CURVATURE CONTRIBUTIONS TO THE ELASTIC ENERGY

While our atomic relaxation model is restricted to in-plane relaxation, we argue that the most important contributions of out-of-plane strain are still captured. During the DFT calculations of the GSFE function, the interlayer spacing is relaxed separately for each stacking configuration. The result is a map of the GSFE function $V_{\text{GSFE}}(v, w)$, but also a stacking-dependent interlayer spacing function $d(v, w)$. The only effect that is omitted in this calculation is the contribution to the elastic energy emanating from the bending of the membrane. The bending energy can be written as $E_b = \int d^2r (\frac{1}{2} \kappa H^2 + \kappa_G K)$ [92], where H and K are the mean and Gaussian curvatures, respectively, and their respective rigidities κ and κ_G . Similar to Ref. [92], we approximate H and K as $H \approx \nabla^2 f$ and $K \approx \det(\partial_i \partial_j f)$, where f is the out-of-plane strain of the membrane. For the sake of the estimate, we assume $f \approx d$, namely, that the

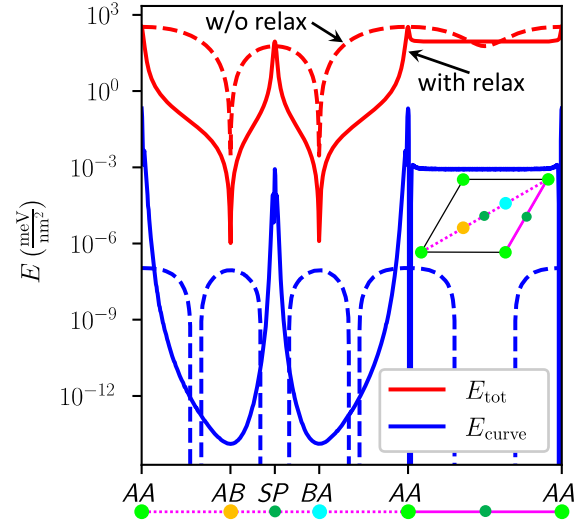


FIG. 8. Effects of curvature on atomic relaxation process in twisted-bilayer graphene. Comparing total energy density (red) to the elastic energy term resulting from membrane bending (blue; more details in the text) before and after relaxation (dashed and solid lines, respectively) as a function of the original (before relaxation) stacking configuration (on a path in configuration space indicated in the inset). The out-of-plane displacement is taken to be the layer spacing at the local configuration as presented in Table III of Ref. [94] (and independently corroborated).

TABLE II. Material parameters for the PdTe₂/Bi₂Se₃ and graphene-based heterostructures used for the relaxation calculations in this work. $c_{0,\dots,5}$ are the GSF coefficients of Eq. (10) for the PdTe₂/PdTe₂, Bi₂Se₃/Bi₂Se₃, PdTe₂/Bi₂Se₃, and the graphene-graphene interfaces (u.c. stands for the area of the 2D unit cell). α are the lattice constants for PdTe₂, Bi₂Se₃, and graphene. K and G stand for the bulk and shear moduli.

	PdTe ₂	Bi ₂ Se ₃	PdTe ₂ /Bi ₂ Se ₃	Graphene
c_0 ($\frac{\text{meV}}{\text{u.c.}}$)	157.73	59.19	102.65	6.832
c_1 ($\frac{\text{meV}}{\text{u.c.}}$)	-41.10	22.80	28.21	4.064
c_2 ($\frac{\text{meV}}{\text{u.c.}}$)	-6.25	-4.76	-6.47	-0.374
c_3 ($\frac{\text{meV}}{\text{u.c.}}$)	-5.23	-0.21	-1.66	-0.095
c_4 ($\frac{\text{meV}}{\text{u.c.}}$)	5.63	1.71	11.17	0
c_5 ($\frac{\text{meV}}{\text{u.c.}}$)	1.18	2.53	5.54	0
α (Å)	4.014	4.129		2.47
K ($\frac{\text{meV}}{\text{u.c.}}$)	30 902	47 049		69 518
G ($\frac{\text{meV}}{\text{u.c.}}$)	17 759	25 995		47 352

shape of the membrane is dictated by the local stacking configuration. Only if the curvature-related terms of the elastic energy density are significant relative to the total energy density at a given stacking configuration can one argue that this effect is of importance in the atomic relaxation process. Fig. 8 compares the curvature terms using the above assumptions with the total energy omitting this effect, before and after relaxation. It is clear that the curvature contribution is secondary; therefore, we omit these terms to greatly simplify the model. However, there is no fundamental problem preventing us from including this effect in the model. In the estimate of Fig. 8, we take $\kappa = \kappa_G = 10$ eV following the calculations of Ref. [93] and the material parameters for graphene detailed in Table II.

APPENDIX D: MATERIAL PARAMETERS USED FOR THE RELAXATION CALCULATIONS

The material parameters used for the multilayer graphene relaxations, consisting of the GSF coefficients $c_{0,\dots,5}$ and strain (bulk and shear) moduli K and G , are taken from Ref. [69]. For the PdTe₂/Bi₂Se₃ multilayer simulations, the three interfacial GSF functionals, strain moduli, and monolayer lattice parameters are extracted from density-functional calculations performed with the Vienna *Ab Initio* Simulation Package [95]. A monolayer geometry is used to calculate the α , K , and G values for both materials, and a two-layer geometry is used for the three different GSFs (PdTe₂/PdTe₂, PdTe₂/Bi₂Se₃, and Bi₂Se₃/Bi₂Se₃). The numerical values of all material parameters relevant for relaxing the atomic structures are given in Table II. In all cases, the out-of-plane c axis (parallel to z) is set to 30 Å to ensure no interaction between the periodic slabs. The van der Waals energy functional SCAN + rVV10 [96] is used

alongside PAW-PBE pseudo potentials for all atoms [97]. A plane-wave energy cutoff of 300 eV and electronic convergence of 10^{-5} eV are used, with dipole corrections turned on for the out-of-plane (c , or z) axis. Optimization of the lattice constant for the monolayer, and out-of-plane relaxation of the atoms for the interfacial calculations, are performed via conjugate-gradient descent with a 10^{-4} -eV convergence criterion.

APPENDIX E: LDOS FROM THE CONTINUUM MODEL

Spectral densities generally can be defined in an arbitrary basis of the Hamiltonian. The layer-resolved local density of states, i.e., LDOS(l, ω, \mathbf{r}), is nothing else but the spectral density in a basis consisting of real-space, layer, sublattice, valley, and momentum indices. The sublattice (x), valley, and momentum degrees of freedom are summed over to obtain a function of l and \mathbf{r} , and frequency ω . As our model Eq. (32) is formulated in reciprocal moiré lattice vector (\mathbf{G}) space, we obtain the following Green's function:

$$G^{GG', \xi, l', xx'}(i\omega, \mathbf{k}) = \sum_b \frac{u_{\mathbf{G}, \xi, l, x}^b(\mathbf{k}) [u_{\mathbf{G}', \xi, l', x'}^b(\mathbf{k})]^*}{i\omega - \epsilon_{\xi}^b(\mathbf{k})}, \quad (\text{E1})$$

with b a band index and $\epsilon_{\xi}^b(\mathbf{k})$ the dispersion of band b of valley ξ at momentum \mathbf{k} . Note that, since the Hamiltonian is diagonal in the valleys $\xi = \pm 1$, the Green's function carries only one valley index as well. For a real-space description, we need to transform the \mathbf{G} indices to real space:

$$G^{rr', \xi, ll', xx'}(i\omega, \mathbf{k}) = \frac{1}{N_G} \sum_{\mathbf{G}\mathbf{G}'} e^{-i(\mathbf{G}\mathbf{r} - \mathbf{G}'\mathbf{r}')} G^{GG', \xi, ll', xx'}(i\omega, \mathbf{k}). \quad (\text{E2})$$

Here, the number of reciprocal moiré lattice vectors N_G is needed for proper normalization. The representation in a diagonal basis, Eq. (E1), numerically facilitates the Fourier transform: Instead of transforming both indices in a double sum [cf. Eq. (E2)], we can directly transform the ‘‘Bloch’’ functions $u_{\mathbf{G}, \xi, l, x}^b(\mathbf{k})$ to real space:

$$u_{\mathbf{r}, \xi, l, x}^b(\mathbf{k}) = \frac{1}{\sqrt{N_G}} \sum_{\mathbf{G}} e^{-i\mathbf{G}\mathbf{r}} u_{\mathbf{G}, \xi, l, x}^b(\mathbf{k}). \quad (\text{E3})$$

Then, we perform the analytic continuation $i\omega \rightarrow \omega + i\eta$ and trace out the sublattice, valley, and momentum indices to arrive at

$$\text{LDOS}(l, \omega, \mathbf{r}) = -\text{Im} \sum_{\xi, x, \mathbf{k}, b} \frac{|u_{\mathbf{r}, \xi, l, x}^b(\mathbf{k})|^2}{\epsilon_{\xi}^b(\mathbf{k}) - \omega + i\eta}. \quad (\text{E4})$$

The broadening parameter η determines the energy resolution. We set $\eta = 5$ meV for all simulations of the $\theta = 0.8^\circ$ systems and $\eta = 0.8$ meV for the $\theta = 0.1^\circ$ case.

The momentum summation is carried out on an equispaced mesh with 14×14 points in a C_3 reduced wedge of the Brillouin zone.

For numerical calculations of the system's electronic properties, we employ a specialized code operating on a hybrid CPU and multi-GPU (OpenMP and CUDA) architecture. Convergence of the inverse moiré lattice vector expansion dictates large matrix sizes for the Hamiltonian. The expansion's cutoff G_c is set by magnitude $\|\mathbf{G}\| < G_c$. In the case of $\theta = 0.1^\circ$, we require $G_c = 13\|\mathbf{B}_{1/2}\|$ for convergence resulting in Hamilton matrix sizes of approximately 50000 (for $n_1 = n_2 = 20$). In the large-angle case ($\theta = 0.8^\circ$), we set $G_c = 5\|\mathbf{B}_{1/2}\|$ to converge the expansion.

APPENDIX F: ADDITIONAL ELECTRONIC STRUCTURE DATA

1. Small-angle case with few-layered graphene

Here we present the additional cases of $n_2 = 3$, $n_2 = 4$, and $n_2 = 6$ for the small-angle ($\theta = 0.1^\circ$) system with

$n_1 = 20$. Figure 9 displays the results in the same manner as Fig. 5 in the main text.

The Figs. 9(a)–9(f) correspond to the LDOS data of the rigid and relaxed systems at $n_2 = 3$, $n_2 = 4$, and $n_2 = 6$. The left subpanel shows the spatially integrated LDOS of the outermost layer with color coding as the coefficient of variation (over space). Here, black corresponds to small variation, i.e., a uniform LDOS, and green corresponds to large variation, i.e., a spatially nonuniform LDOS. Additionally, we add the minimum and maximum values taken by the top-layer LDOS as gray background. At selected frequencies, we show the explicit spatial distribution of the LDOS for each system on the right-hand side in the same row. The color maps of the LDOS maps are normalized for the rigid and relaxed cases of a single n_2 , i.e., subsequent rows [e.g., Figs. 9(a) and 9(b)] share a color-map normalization. The color scheme of the LDOS maps evolves as a function of the frequency to match the color of the vertical dashed lines indicating the exact frequency values. Even in the few-layer (small-angle) data in Fig. 9, we observe the tendency that, when increasing n_2 ,

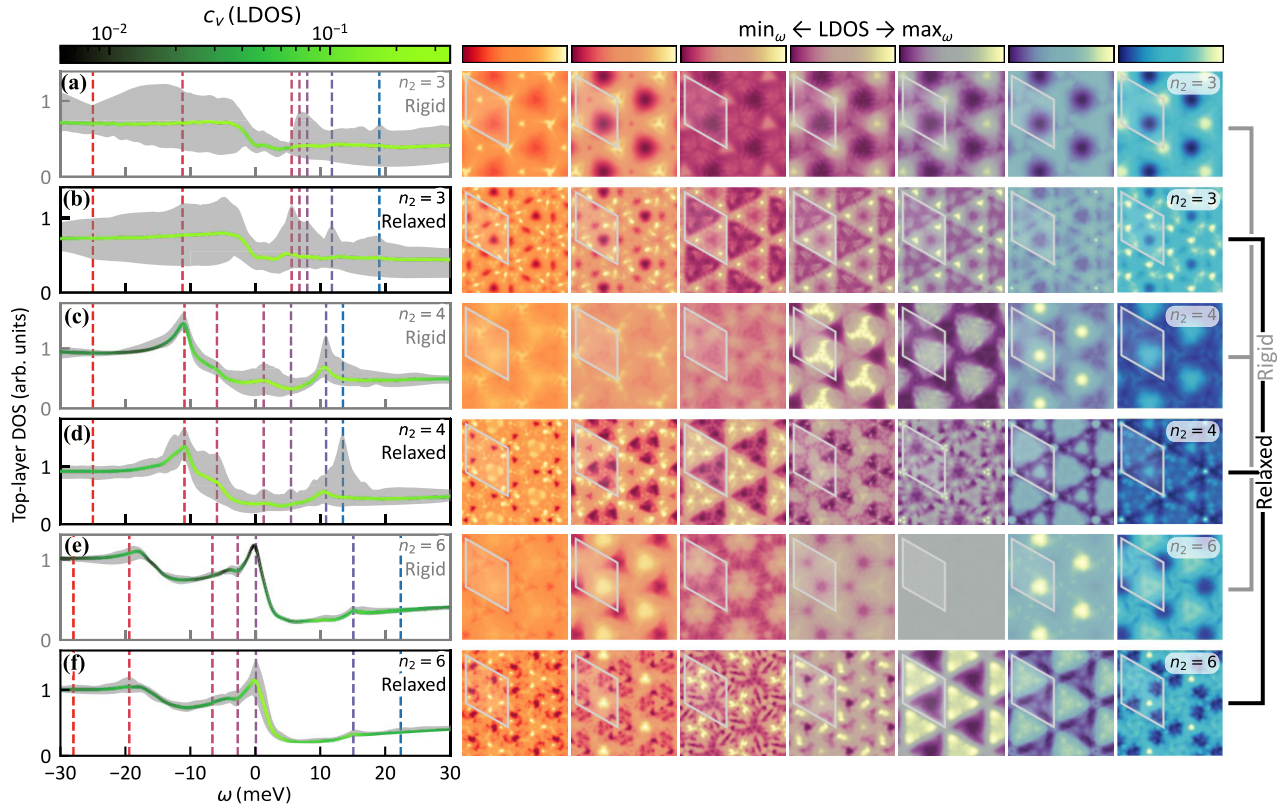


FIG. 9. Small-angle ($\theta = 0.1^\circ$) electronic structure of few-layer graphene on graphite. The number of layers of the first graphite flake is set to $n_1 = 20$, whereas the number of layers of the second graphite flake is varied from $n_2 = 3$ (a),(b) over $n_2 = 4$ (c),(d) to $n_2 = 6$ (e),(f). In panels (rows) (a),(c),(e) we use rigid atomic positions and in (b),(d),(f) relaxed ones. The color of the lines in the left subpanels codes the coefficient of the variation of the top-layer LDOS, with green as nonuniform regions and black as uniform regions. The gray background is given by the minimum and maximum values of the LDOS. On the right, we show LDOS maps at selected frequencies indicated in the left subpanels. Each subsequent two rows [e.g., (a) and (b)] share a color map for each frequency such that differences in relaxed and rigid structures are apparent.

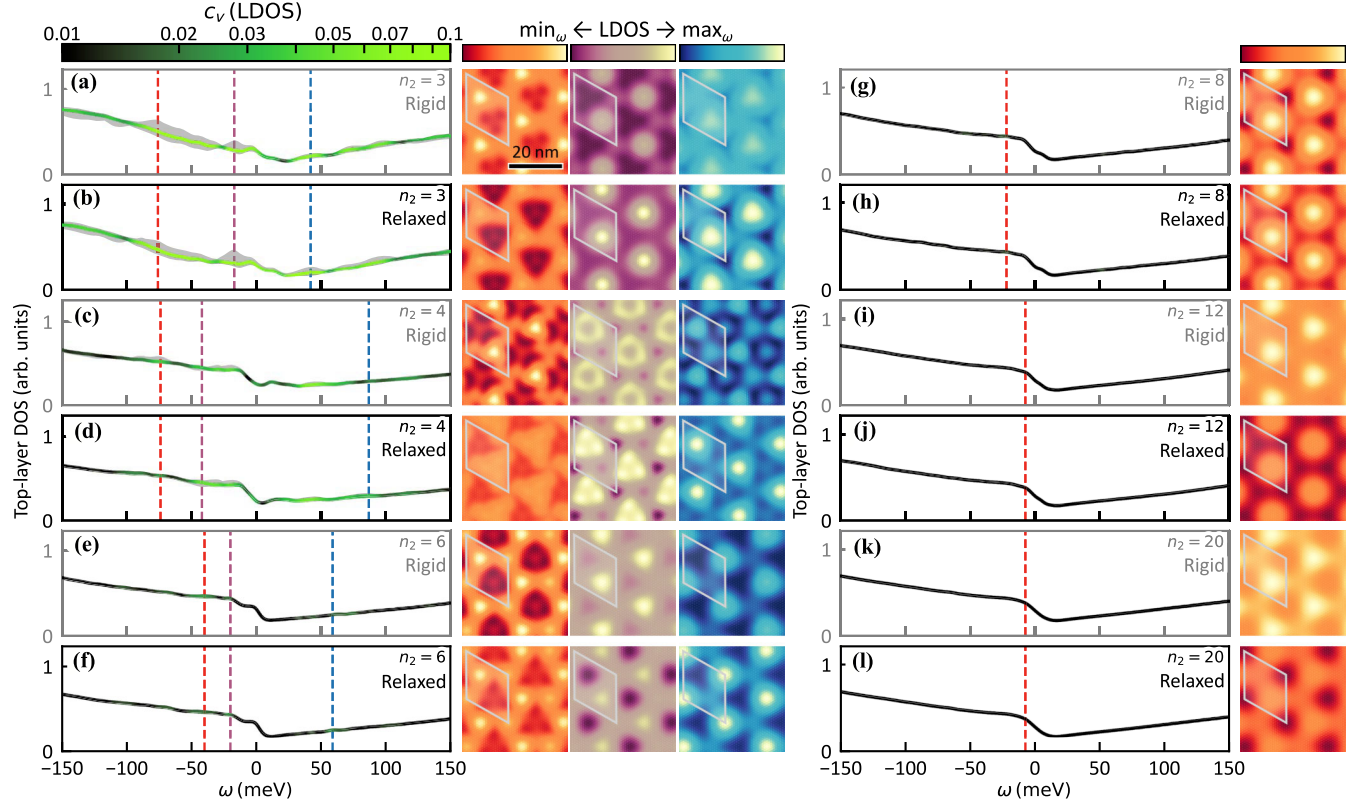


FIG. 10. Overview of electronic structure of many-layer graphene twisted at $\theta = 0.8^\circ$ on a graphite system. Similar to Fig. 5 and 9, we display the integrated top-layer DOS and additionally color code the coefficient of variation c_v . Furthermore, we mark the minimum and maximum values taken by the top-layer LDOS as gray background. The system considered here also consists of $n_1 = 20$ layers of graphene as a bottom flake and $n_2 = 3, \dots, 20$ layers of graphene as a top flake. In (a)–(f), we vary n_2 from 3 over 4 to 6, with subsequent rows corresponding to the relaxed and rigid cases of the same system. The subpanels on the right show the LDOS maps at selected frequencies indicated as vertical dashed lines in the left subpanels. The color maps correspond to the vertical dashed lines’ colors. Two subsequent rows [e.g., (a) and (b)] share a color map for each frequency to make differences apparent. (g)–(l) Same as panels (a)–(f), but for $n_2 = 8, n_2 = 12$, and $n_2 = 20$. As for these systems, the local variations in the electronic density of the top layer are very minuscule, we show only the LDOS maps at a single frequency. Apart from a small shift in absolute scale, these LDOS maps are very similar between each relaxed and rigid case in panels (g)–(l).

the local variations in top-layer LDOS are strongly enhanced for the relaxed case.

2. Large-angle case

To highlight the importance of small twist angles for large penetration depths of relaxation effects into the stack, here we present the analysis of the electronic structure for a twist angle of $\theta = 0.8^\circ$. As in Sec. V and Appendix F 1, the number of graphene layers in the bottom flake is fixed at $n_1 = 20$, and we vary the number of graphene layers in the top flake from $n_2 = 3$ to $n_2 = 20$. The results are presented in Figure 10. Overall, we observe that patterns in the LDOS of the top layer decay much faster as a function of increasing n_2 . For example, even the $n_2 = 6$ and $n_2 = 8$ cases display no notable difference in c_v of the relaxed and rigid structures. For $n_2 \geq 8$, the value of c_v is too small to be visible on the selected scale (less than 1%). Furthermore, no such clear pattern of increased c_v in the relaxed case

over the rigid case can be found as for the small-angle ($\theta = 0.1^\circ$) case. We interpret this behavior as the relaxation decaying as fast—or faster than—the effects that the moiré interlayer coupling $U^{G,G'}$ has on the top-layer electronic structure.

3. Full frequency LDOS maps

As Supplemental Material [73], we provide all LDOS maps for the systems studied within this work as videos where we change ω with each frame. The color maps evolve as a function of ω similar to the color maps of the LDOS maps in Figs. 5, 9, and 10. The upper panel corresponds to the rigid structure and the lower panel to the relaxed one. In each frame, we normalize the color map separately with bright (yellow) colors indicating maxima and dark (red and blue) colors indicating minima. To display only significant LDOS variations in the videos, we set the minimum relative difference that needs to be

covered by the color map to $\pm 2\%$ such that when the minimum and maximum values are closer than 2% to their mean value, we artificially increase the color-mapped minimum and maximum values to be 2% away from the mean value.

-
- [1] M. Wang, S. K. Jang, W.-J. Jang, M. Kim, S.-Y. Park, S.-W. Kim, S.-J. Kahng, J.-Y. Choi, R. S. Ruoff, Y. J. Song, and S. Lee, *A Platform for Large-Scale Graphene Electronics—CVD Growth of Single-Layer Graphene on CVD-Grown Hexagonal Boron Nitride*, *Adv. Mater.* **25**, 2746 (2013).
- [2] H. Wang, F. Liu, W. Fu, Z. Fang, W. Zhou, and Z. Liu, *Two-Dimensional Heterostructures: Fabrication, Characterization, and Application*, *Nanoscale* **6**, 12250 (2014).
- [3] T. Niu and A. Li, *From Two-Dimensional Materials to Heterostructures*, *Prog. Surf. Sci.* **90**, 21 (2015).
- [4] K. Novoselov, A. Mishchenko, A. Carvalho, and A. Castro Neto, *2D Materials and van der Waals Heterostructures*, *Science* **353**, aac9439 (2016).
- [5] Y. Cao, V. Fatemi, S. Fang, K. Watanabe, T. Taniguchi, E. Kaxiras, and P. Jarillo-Herrero, *Unconventional Superconductivity in Magic-Angle Graphene Superlattices*, *Nature (London)* **556**, 43 (2018).
- [6] X. Lu, P. Stepanov, W. Yang, M. Xie, M. A. Aamir, I. Das, C. Urgell, K. Watanabe, T. Taniguchi, G. Zhang, A. Bachtold, A. H. MacDonald, and D. K. Efetov, *Superconductors, Orbital Magnets and Correlated States in Magic-Angle Bilayer Graphene*, *Nature (London)* **574**, 653 (2019).
- [7] M. Yankowitz, S. Chen, H. Polshyn, Y. Zhang, K. Watanabe, T. Taniguchi, D. Graf, A. F. Young, and C. R. Dean, *Tuning Superconductivity in Twisted Bilayer Graphene*, *Science* **363**, 1059 (2019).
- [8] Y. Cao, D. Rodan-Legrain, J. M. Park, F. N. Yuan, K. Watanabe, T. Taniguchi, R. M. Fernandes, L. Fu, and P. Jarillo-Herrero, *Nematicity and Competing Orders in Superconducting Magic-Angle Graphene*, [arXiv:2004.04148](https://arxiv.org/abs/2004.04148).
- [9] X. Liu, Z. Wang, K. Watanabe, T. Taniguchi, O. Vafek, and J. Li, *Tuning Electron Correlation in Magic-Angle Twisted Bilayer Graphene Using Coulomb Screening*, *Science* **371**, 1261 (2021).
- [10] P. Stepanov, I. Das, X. Lu, A. Fahimniya, K. Watanabe, T. Taniguchi, F. H. Koppens, J. Lischner, L. Levitov, and D. K. Efetov, *Untying the Insulating and Superconducting Orders in Magic-Angle Graphene*, *Nature (London)* **583**, 375 (2020).
- [11] H. S. Arora, R. Polski, Y. Zhang, A. Thomson, Y. Choi, H. Kim, Z. Lin, I. Z. Wilson, X. Xu, J.-H. Chu *et al.*, *Superconductivity in Metallic Twisted Bilayer Graphene Stabilized by WSe₂*, *Nature (London)* **583**, 379 (2020).
- [12] M. Oh, K. P. Nuckolls, D. Wong, R. L. Lee, X. Liu, K. Watanabe, T. Taniguchi, and A. Yazdani, *Evidence for Unconventional Superconductivity in Twisted Bilayer Graphene*, *Nature (London)* **600**, 240 (2021).
- [13] J. M. Park, Y. Cao, K. Watanabe, T. Taniguchi, and P. Jarillo-Herrero, *Tunable Strongly Coupled Superconductivity in Magic-Angle Twisted Trilayer Graphene*, *Nature (London)* **590**, 249 (2021).
- [14] Y. Cao, J. M. Park, K. Watanabe, T. Taniguchi, and P. Jarillo-Herrero, *Pauli-Limit Violation and Re-entrant Superconductivity in Moiré Graphene*, *Nature (London)* **595**, 526 (2021).
- [15] Z. Hao, A. Zimmerman, P. Ledwith, E. Khalaf, D. H. Najafabadi, K. Watanabe, T. Taniguchi, A. Vishwanath, and P. Kim, *Electric Field-Tunable Superconductivity in Alternating-Twist Magic-Angle Trilayer Graphene*, *Science* **371**, 1133 (2021).
- [16] H. Kim, Y. Choi, C. Lewandowski, A. Thomson, Y. Zhang, R. Polski, K. Watanabe, T. Taniguchi, J. Alicea, and S. Nadj-Perge, *Spectroscopic Signatures of Strong Correlations and Unconventional Superconductivity in Twisted Trilayer Graphene*, [arXiv:2109.12127](https://arxiv.org/abs/2109.12127).
- [17] Y. Cao, V. Fatemi, A. Demir, S. Fang, S. L. Tomarken, J. Y. Luo, J. D. Sanchez-Yamagishi, K. Watanabe, T. Taniguchi, E. Kaxiras, R. C. Ashoori, and P. Jarillo-Herrero, *Correlated Insulator Behaviour at Half-Filling in Magic-Angle Graphene Superlattices*, *Nature (London)* **556**, 80 (2018).
- [18] Y. Cao, D. Chowdhury, D. Rodan-Legrain, O. Rubies-Bigordà, K. Watanabe, T. Taniguchi, T. Senthil, and P. Jarillo-Herrero, *Strange Metal in Magic-Angle Graphene with near Planckian Dissipation*, *Phys. Rev. Lett.* **124**, 076801 (2020).
- [19] H. Polshyn, M. Yankowitz, S. Chen, Y. Zhang, K. Watanabe, T. Taniguchi, C. R. Dean, and A. F. Young, *Large Linear-in-Temperature Resistivity in Twisted Bilayer Graphene*, *Nat. Phys.* **15**, 1011 (2019).
- [20] U. Zondiner, A. Rozen, D. Rodan-Legrain, Y. Cao, R. Queiroz, T. Taniguchi, K. Watanabe, Y. Oreg, F. von Oppen, A. Stern, E. Berg, P. Jarillo-Herrero, and S. Ilani, *Cascade of Phase Transitions and Dirac Revivals in Magic-Angle Graphene*, *Nature (London)* **582**, 203 (2020).
- [21] D. Wong, K. P. Nuckolls, M. Oh, B. Lian, S. J. Yonglong Xie, K. Watanabe, T. Taniguchi, B. A. Bernevig, and A. Yazdani, *Cascade of Electronic Transitions in Magic-Angle Twisted Bilayer Graphene*, *Nature (London)* **582**, 198 (2020).
- [22] Y. Xie, B. Lian, B. Jäck, X. Liu, C.-L. Chiu, K. Watanabe, T. Taniguchi, B. A. Bernevig, and A. Yazdani, *Spectroscopic Signatures of Many-Body Correlations in Magic-Angle Twisted Bilayer Graphene*, *Nature (London)* **572**, 101 (2019).
- [23] A. Kerelsky, L. J. McGilly, D. M. Kennes, L. Xian, M. Yankowitz, S. Chen, K. Watanabe, T. Taniguchi, J. Hone, C. Dean, A. Rubio, and A. N. Pasupathy, *Maximized Electron Interactions at the Magic Angle in Twisted Bilayer Graphene*, *Nature (London)* **572**, 95 (2019).
- [24] Y. Jiang, X. Lai, K. Watanabe, T. Taniguchi, K. Haule, J. Mao, and E. Y. Andrei, *Charge Order and Broken Rotational Symmetry in Magic-Angle Twisted Bilayer Graphene*, *Nature (London)* **573**, 91 (2019).
- [25] Y. Choi, J. Kemmer, Y. Peng, A. Thomson, H. Arora, R. Polski, Y. Zhang, H. Ren, J. Alicea, G. Refael, F. von Oppen, K. Watanabe, T. Taniguchi, and S. Nadj-Perge, *Electronic Correlations in Twisted Bilayer Graphene near the Magic Angle*, *Nat. Phys.* **15**, 1174 (2019).
- [26] S. Chen, M. He, Y.-H. Zhang, V. Hsieh, Z. Fei, K. Watanabe, T. Taniguchi, D. H. Cobden, X. Xu, C. R. Dean *et al.*, *Electrically Tunable Correlated and Topological States in*

- Twisted Monolayer–Bilayer Graphene*, *Nat. Phys.* **17**, 374 (2021).
- [27] Y. Shi, S. Xu, M. M. A. Ezzi, N. Balakrishnan, A. Garcia-Ruiz, B. Tsim, C. Mullan, J. Barrier, N. Xin, B. A. Piot *et al.*, *Tunable van Hove Singularities and Correlated States in Twisted Trilayer Graphene*, *Nat. Phys.* **17**, 619 (2021).
- [28] X. Liu, Z. Hao, E. Khalaf, J. Y. Lee, Y. Ronen, H. Yoo, D. Haei Najafabadi, K. Watanabe, T. Taniguchi, A. Vishwanath *et al.*, *Tunable Spin-Polarized Correlated States in Twisted Double Bilayer Graphene*, *Nature (London)* **583**, 221 (2020).
- [29] C. Shen, Y. Chu, Q. Wu, N. Li, S. Wang, Y. Zhao, J. Tang, J. Liu, J. Tian, K. Watanabe *et al.*, *Correlated States in Twisted Double Bilayer Graphene*, *Nat. Phys.* **16**, 520 (2020).
- [30] Y. Cao, D. Rodan-Legrain, O. Rubies-Bigorda, J. M. Park, K. Watanabe, T. Taniguchi, and P. Jarillo-Herrero, *Tunable Correlated States and Spin-Polarized Phases in Twisted Bilayer–Bilayer Graphene*, *Nature (London)* **583**, 215 (2020).
- [31] L. Wang, E.-M. Shih, A. Ghiotto, L. Xian, D. A. Rhodes, C. Tan, M. Claassen, D. M. Kennes, Y. Bai, B. Kim *et al.*, *Correlated Electronic Phases in Twisted Bilayer Transition Metal Dichalcogenides*, *Nat. Mater.* **19**, 861 (2020).
- [32] Y. Tang, L. Li, T. Li, Y. Xu, S. Liu, K. Barmak, K. Watanabe, T. Taniguchi, A. H. MacDonald, J. Shan *et al.*, *Simulation of Hubbard Model Physics in WSe_2/WS_2 Moiré Superlattices*, *Nature (London)* **579**, 353 (2020).
- [33] E. C. Regan, D. Wang, C. Jin, M. I. Bakti Utama, B. Gao, X. Wei, S. Zhao, W. Zhao, Z. Zhang, K. Yumigeta *et al.*, *Mott and Generalized Wigner Crystal States in WSe_2/WS_2 Moiré Superlattices*, *Nature (London)* **579**, 359 (2020).
- [34] P. K. Nayak, Y. Horbatenko, S. Ahn, G. Kim, J.-U. Lee, K. Y. Ma, A.-R. Jang, H. Lim, D. Kim, S. Ryu *et al.*, *Probing Evolution of Twist-Angle-Dependent Interlayer Excitons in $MoSe_2/WSe_2$ van der Waals Heterostructures*, *ACS Nano* **11**, 4041 (2017).
- [35] P. Rivera, H. Yu, K. L. Seyler, N. P. Wilson, W. Yao, and X. Xu, *Interlayer Valley Excitons in Heterobilayers of Transition Metal Dichalcogenides*, *Nat. Nanotechnol.* **13**, 1004 (2018).
- [36] E. M. Alexeev, D. A. Ruiz-Tijerina, M. Danovich, M. J. Hamer, D. J. Terry, P. K. Nayak, S. Ahn, S. Pak, J. Lee, J. I. Sohn *et al.*, *Resonantly Hybridized Excitons in Moiré Superlattices in van der Waals Heterostructures*, *Nature (London)* **567**, 81 (2019).
- [37] T. I. Andersen, G. Scuri, A. Sushko, K. De Greve, J. Sung, Y. Zhou, D. S. Wild, R. J. Gelly, H. Heo, D. Bérubé *et al.*, *Excitons in a Reconstructed Moiré Potential in Twisted WSe_2/WSe_2 Homobilayers*, *Nat. Mater.* **20**, 480 (2021).
- [38] C. Jin, E. C. Regan, A. Yan, M. Iqbal Bakti Utama, D. Wang, S. Zhao, Y. Qin, S. Yang, Z. Zheng, S. Shi *et al.*, *Observation of Moiré Excitons in WSe_2/WS_2 Heterostructure Superlattices*, *Nature (London)* **567**, 76 (2019).
- [39] G. W. Burg, J. Zhu, T. Taniguchi, K. Watanabe, A. H. MacDonald, and E. Tutuc, *Correlated Insulating States in Twisted Double Bilayer Graphene*, *Phys. Rev. Lett.* **123**, 197702 (2019).
- [40] C. Rubio-Verdú, S. Turkel, Y. Song, L. Klebl, R. Samajdar, M. S. Scheurer, J. W. Venderbos, K. Watanabe, T. Taniguchi, H. Ochoa *et al.*, *Moiré Nematic Phase in Twisted Double Bilayer Graphene*, *Nat. Phys.* **18**, 196 (2022).
- [41] G. Chen, A. L. Sharpe, P. Gallagher, I. T. Rosen, E. J. Fox, L. Jiang, B. Lyu, H. Li, K. Watanabe, T. Taniguchi *et al.*, *Signatures of Tunable Superconductivity in a Trilayer Graphene Moiré Superlattice*, *Nature (London)* **572**, 215 (2019).
- [42] G. Chen, L. Jiang, S. Wu, B. Lyu, H. Li, B. L. Chittari, K. Watanabe, T. Taniguchi, Z. Shi, J. Jung *et al.*, *Evidence of a Gate-Tunable Mott Insulator in a Trilayer Graphene Moiré Superlattice*, *Nat. Phys.* **15**, 237 (2019).
- [43] G. Chen, A. L. Sharpe, E. J. Fox, Y.-H. Zhang, S. Wang, L. Jiang, B. Lyu, H. Li, K. Watanabe, T. Taniguchi *et al.*, *Tunable Correlated Chern Insulator and Ferromagnetism in a Moiré Superlattice*, *Nature (London)* **579**, 56 (2020).
- [44] K. P. Nuckolls, M. Oh, D. Wong, B. Lian, K. Watanabe, T. Taniguchi, B. A. Bernevig, and A. Yazdani, *Strongly Correlated Chern Insulators in Magic-Angle Twisted Bilayer Graphene*, *Nature (London)* **588**, 610 (2020).
- [45] Y. Xie, A. T. Pierce, J. M. Park, D. E. Parker, E. Khalaf, P. Ledwith, Y. Cao, S. H. Lee, S. Chen, P. R. Forrester *et al.*, *Fractional Chern Insulators in Magic-Angle Twisted Bilayer Graphene*, *Nature (London)* **600**, 439 (2021).
- [46] A. T. Pierce, Y. Xie, J. M. Park, E. Khalaf, S. H. Lee, Y. Cao, D. E. Parker, P. R. Forrester, S. Chen, K. Watanabe *et al.*, *Unconventional Sequence of Correlated Chern Insulators in Magic-Angle Twisted Bilayer Graphene*, *Nat. Phys.* **17**, 1210 (2021).
- [47] P. Stepanov, M. Xie, T. Taniguchi, K. Watanabe, X. Lu, A. H. MacDonald, B. A. Bernevig, and D. K. Efetov, *Competing Zero-Field Chern Insulators in Superconducting Twisted Bilayer Graphene*, *Phys. Rev. Lett.* **127**, 197701 (2021).
- [48] Y. Choi, H. Kim, Y. Peng, A. Thomson, C. Lewandowski, R. Polski, Y. Zhang, H. S. Arora, K. Watanabe, T. Taniguchi *et al.*, *Tracing Out Correlated Chern Insulators in Magic Angle Twisted Bilayer Graphene*, arXiv:2008.11746.
- [49] A. L. Sharpe, E. J. Fox, A. W. Barnard, J. Finney, K. Watanabe, T. Taniguchi, M. Kastner, and D. Goldhaber-Gordon, *Emergent Ferromagnetism near Three-Quarters Filling in Twisted Bilayer Graphene*, *Science* **365**, 605 (2019).
- [50] S. Wu, Z. Zhang, K. Watanabe, T. Taniguchi, and E. Y. Andrei, *Chern Insulators, van Hove Singularities and Topological Flat Bands in Magic-Angle Twisted Bilayer Graphene*, *Nat. Mater.* **20**, 488 (2021).
- [51] I. Das, X. Lu, J. Herzog-Arbeitman, Z.-D. Song, K. Watanabe, T. Taniguchi, B. A. Bernevig, and D. K. Efetov, *Symmetry-Broken Chern Insulators and Rashba-like Landau-Level Crossings in Magic-Angle Bilayer Graphene*, *Nat. Phys.* **17**, 710 (2021).
- [52] J. M. Park, Y. Cao, K. Watanabe, T. Taniguchi, and P. Jarillo-Herrero, *Flavour Hund’s Coupling, Chern Gaps and Charge Diffusivity in Moiré Graphene*, *Nature (London)* **592**, 43 (2021).
- [53] Y. Saito, J. Ge, K. Watanabe, T. Taniguchi, and A. F. Young, *Independent Superconductors and Correlated Insulators in Twisted Bilayer Graphene*, *Nat. Phys.* **16**, 926 (2020).
- [54] D. M. Kennes, M. Claassen, L. Xian, A. Georges, A. J. Millis, J. Hone, C. R. Dean, D. N. Basov, A. N. Pasupathy, and A. Rubio, *Moiré Heterostructures as a Condensed-Matter Quantum Simulator*, *Nat. Phys.* **17**, 155 (2021).

- [55] S. Carr, S. Fang, and E. Kaxiras, *Electronic-Structure Methods for Twisted Moiré Layers*, *Nat. Rev. Mater.* **5**, 748 (2020).
- [56] A. K. Geim and I. V. Grigorieva, *van der Waals Heterostructures*, *Nature (London)* **499**, 419 (2013).
- [57] K. Uchida, S. Furuya, J.-I. Iwata, and A. Oshiyama, *Atomic Corrugation and Electron Localization Due to Moiré Patterns in Twisted Bilayer Graphenes*, *Phys. Rev. B* **90**, 155451 (2014).
- [58] P. Lucignano, D. Alfè, V. Cataudella, D. Ninno, and G. Cantele, *Crucial Role of Atomic Corrugation on the Flat Bands and Energy Gaps of Twisted Bilayer Graphene at the Magic Angle $\theta \sim 1.08^\circ$* , *Phys. Rev. B* **99**, 195419 (2019).
- [59] F. Guinea and N. R. Walet, *Continuum Models for Twisted Bilayer Graphene: The Effects of Lattice Deformation and Hopping Parameters*, *Phys. Rev. B* **99**, 205134 (2019).
- [60] G. Cantele, D. Alfè, F. Conte, V. Cataudella, D. Ninno, and P. Lucignano, *Structural Relaxation and Low Energy Properties of Twisted Bilayer Graphene*, *Phys. Rev. Res.* **2**, 043127 (2020).
- [61] L. J. McGilly *et al.*, *Visualization of Moiré Superlattices*, *Nat. Nanotechnol.* **15**, 580 (2020).
- [62] J. Cook, D. Halbertal, Q. Lu, M. Snyder, Y. S. Hor, D. N. Basov, and G. Bian, *Moiré Modulated Lattice Strain and Thickness-Dependent Lattice Expansion in Epitaxial Ultrathin Films of PdTe₂*, arXiv:2206.07035.
- [63] M. H. Naik and M. Jain, *Ultraflatbands and Shear Solitons in Moiré Patterns of Twisted Bilayer Transition Metal Dichalcogenides*, *Phys. Rev. Lett.* **121**, 266401 (2018).
- [64] F. Gargiulo and O. V. Yazyev, *Structural and Electronic Transformation in Low-Angle Twisted Bilayer Graphene*, *2D Mater.* **5**, 015019 (2018).
- [65] F. Haddadi, Q. S. Wu, A. J. Kruchkov, and O. V. Yazyev, *Moiré Flat Bands in Twisted Double Bilayer Graphene*, *Nano Lett.* **20**, 2410 (2020).
- [66] M. Van Wijk, A. Schuring, M. Katsnelson, and A. Fasolino, *Relaxation of Moiré Patterns for Slightly Misaligned Identical Lattices: Graphene on Graphite*, *2D Mater.* **2**, 034010 (2015).
- [67] I. Maity, P. K. Maiti, H. R. Krishnamurthy, and M. Jain, *Reconstruction of Moiré Lattices in Twisted Transition Metal Dichalcogenide Bilayers*, *Phys. Rev. B* **103**, L121102 (2021).
- [68] S. K. Jain, V. Juričić, and G. T. Barkema, *Structure of Twisted and Buckled Bilayer Graphene*, *2D Mater.* **4**, 015018 (2016).
- [69] S. Carr, D. Massatt, S. B. Torrisi, P. Cazeaux, M. Luskin, and E. Kaxiras, *Relaxation and Domain Formation in Incommensurate Two-Dimensional Heterostructures*, *Phys. Rev. B* **98**, 224102 (2018).
- [70] Z. Zhu, S. Carr, D. Massatt, M. Luskin, and E. Kaxiras, *Twisted Trilayer Graphene: A Precisely Tunable Platform for Correlated Electrons*, *Phys. Rev. Lett.* **125**, 116404 (2020).
- [71] P. Cazeaux, M. Luskin, and D. Massatt, *Energy Minimization of Two Dimensional Incommensurate Heterostructures*, *Arch. Ration. Mech. Anal.* **235**, 1289 (2020).
- [72] D. Halbertal *et al.*, *Moiré Metrology of Energy Landscapes in van der Waals Heterostructures*, *Nat. Commun.* **12**, 1 (2021).
- [73] See Supplemental Material at <http://link.aps.org/supplemental/10.1103/PhysRevX.13.011026> for videos of the layer dependent moiré lattice constant in PdTe₂ on Bi₂Se₃ (where n_{PdTe_2} is varied with time) and videos of the electronic real-space top-layer spectral function in each of the multilayered graphene structures discussed in the main text (where frequency ω is varied with time).
- [74] S. V. Morozov, K. S. Novoselov, M. I. Katsnelson, F. Schedin, L. A. Ponomarenko, D. Jiang, and A. K. Geim, *Strong Suppression of Weak Localization in Graphene*, *Phys. Rev. Lett.* **97**, 016801 (2006).
- [75] M. Vozmediano, M. Katsnelson, and F. Guinea, *Gauge Fields in Graphene*, *Phys. Rep.* **496**, 109 (2010).
- [76] M. I. Katsnelson, *Graphene: Carbon in Two Dimensions* (Cambridge University Press, Cambridge, England, 2012).
- [77] B. Amorim, A. Cortijo, F. de Juan, A. Grushin, F. Guinea, A. Gutiérrez-Rubio, H. Ochoa, V. Parente, R. Roldán, P. San-Jose, J. Schiefele, M. Sturla, and M. Vozmediano, *Novel Effects of Strains in Graphene and Other Two Dimensional Materials*, *Phys. Rep.* **617**, 1 (2016).
- [78] N. N. T. Nam and M. Koshino, *Lattice Relaxation and Energy Band Modulation in Twisted Bilayer Graphene*, *Phys. Rev. B* **96**, 075311 (2017).
- [79] X. Liang, Z. A. H. Goodwin, V. Vitale, F. Corsetti, A. A. Mostofi, and J. Lischner, *Effect of Bilayer Stacking on the Atomic and Electronic Structure of Twisted Double Bilayer Graphene*, *Phys. Rev. B* **102**, 155146 (2020).
- [80] R. Bistritzer and A. H. MacDonald, *Moiré Bands in Twisted Double-Layer Graphene*, *Proc. Natl. Acad. Sci. U.S.A.* **108**, 12233 (2011).
- [81] J. M. B. Lopes dos Santos, N. M. R. Peres, and A. H. Castro Neto, *Continuum Model of the Twisted Graphene Bilayer*, *Phys. Rev. B* **86**, 155449 (2012).
- [82] J. M. B. Lopes dos Santos, N. M. R. Peres, and A. H. Castro Neto, *Graphene Bilayer with a Twist: Electronic Structure*, *Phys. Rev. Lett.* **99**, 256802 (2007).
- [83] M. Koshino, N. F. Q. Yuan, T. Koretsune, M. Ochi, K. Kuroki, and L. Fu, *Maximally Localized Wannier Orbitals and the Extended Hubbard Model for Twisted Bilayer Graphene*, *Phys. Rev. X* **8**, 031087 (2018).
- [84] T. Cea, N. R. Walet, and F. Guinea, *Twists and the Electronic Structure of Graphitic Materials*, *Nano Lett.* **19**, 8683 (2019).
- [85] L. Balents, *General Continuum Model for Twisted Bilayer Graphene and Arbitrary Smooth Deformations*, *SciPost Phys.* **7**, 48 (2019).
- [86] M. Koshino and N. N. T. Nam, *Effective Continuum Model for Relaxed Twisted Bilayer Graphene and Moiré Electron-Phonon Interaction*, *Phys. Rev. B* **101**, 195425 (2020).
- [87] A. Grüneis, C. Attacalite, L. Wirtz, H. Shiozawa, R. Saito, T. Pichler, and A. Rubio, *Tight-Binding Description of the Quasiparticle Dispersion of Graphite and Few-Layer Graphene*, *Phys. Rev. B* **78**, 205425 (2008).
- [88] M. Koshino, *Band Structure and Topological Properties of Twisted Double Bilayer Graphene*, *Phys. Rev. B* **99**, 235406 (2019).
- [89] R. Samajdar and M. S. Scheurer, *Microscopic Pairing Mechanism, Order Parameter, and Disorder Sensitivity in Moiré Superlattices: Applications to Twisted Double-Bilayer Graphene*, *Phys. Rev. B* **102**, 064501 (2020).

- [90] L. Wang, I. Meric, P. Y. Huang, Q. Gao, Y. Gao, H. Tran, T. Taniguchi, K. Watanabe, L. M. Campos, D. A. Muller, J. Guo, P. Kim, J. Hone, Shepard, and C. R. Dean, *One-Dimensional Electrical Contact to a Two-Dimensional Material*, *Science* **342**, 614 (2013).
- [91] P. Moon and M. Koshino, *Electronic Properties of Graphene/Hexagonal-Boron-Nitride Moiré Superlattice*, *Phys. Rev. B* **90**, 155406 (2014).
- [92] S. Chen and D. C. Chrzan, *Continuum Theory of Dislocations and Buckling in Graphene*, *Phys. Rev. B* **84**, 214103 (2011).
- [93] K. Lai, W.-B. Zhang, F. Zhou, F. Zeng, and B.-Y. Tang, *Bending Rigidity of Transition Metal Dichalcogenide Monolayers from First-Principles*, *J. Phys. D* **49**, 185301 (2016).
- [94] S. Zhou, J. Han, S. Dai, J. Sun, and D. J. Srolovitz, *van der Waals Bilayer Energetics: Generalized Stacking-Fault Energy of Graphene, Boron Nitride, and Graphene/Boron Nitride Bilayers*, *Phys. Rev. B* **92**, 155438 (2015).
- [95] G. Kresse and J. Furthmüller, *Efficient Iterative Schemes for Ab Initio Total-Energy Calculations Using a Plane-Wave Basis Set*, *Phys. Rev. B* **54**, 11169 (1996).
- [96] H. Peng, Z.-H. Yang, J. P. Perdew, and J. Sun, *Versatile van der Waals Density Functional Based on a Meta-Generalized Gradient Approximation*, *Phys. Rev. X* **6**, 041005 (2016).
- [97] G. Kresse and D. Joubert, *From Ultrasoft Pseudopotentials to the Projector Augmented-Wave Method*, *Phys. Rev. B* **59**, 1758 (1999).